

Molecular Bases of Disease:
**Structural and Molecular Basis of the
Peroxynitrite-mediated Nitration and
Inactivation of *Trypanosoma cruzi*
Iron-Superoxide Dismutases (Fe-SODs) A
and B: DISPARATE SUSCEPTIBILITIES
DUE TO THE REPAIR OF TYR35
RADICAL BY CYS83 IN Fe-SODB
THROUGH INTRAMOLECULAR
ELECTRON TRANSFER**

Alejandra Martinez, Gonzalo Peluffo, Ariel A.
Petruk, Martín Hugo, Dolores Piñeyro,
Verónica Demicheli, Diego M. Moreno,
Analía Lima, Carlos Batthyány, Rosario
Durán, Carlos Robello, Marcelo A. Martí,
Nicole Larrieux, Alejandro Buschiazzi,
Madia Trujillo, Rafael Radi and Lucía
Piacenza

J. Biol. Chem. 2014, 289:12760-12778.

doi: 10.1074/jbc.M113.545590 originally published online March 10, 2014



Access the most updated version of this article at doi: [10.1074/jbc.M113.545590](https://doi.org/10.1074/jbc.M113.545590)

Find articles, minireviews, Reflections and Classics on similar topics on the [JBC Affinity Sites](https://www.jbc.org/).

Alerts:

- [When this article is cited](#)
- [When a correction for this article is posted](#)

[Click here](#) to choose from all of JBC's e-mail alerts

This article cites 88 references, 25 of which can be accessed free at
<http://www.jbc.org/content/289/18/12760.full.html#ref-list-1>

Structural and Molecular Basis of the Peroxynitrite-mediated Nitration and Inactivation of *Trypanosoma cruzi* Iron-Superoxide Dismutases (Fe-SODs) A and B

DISPARATE SUSCEPTIBILITIES DUE TO THE REPAIR OF TYR³⁵ RADICAL BY CYS⁸³ IN Fe-SODB THROUGH INTRAMOLECULAR ELECTRON TRANSFER*

Received for publication, December 24, 2013, and in revised form, March 8, 2014. Published, JBC Papers in Press, March 10, 2014, DOI 10.1074/jbc.M113.545590

Alejandra Martínez^{‡1}, Gonzalo Peluffo[‡], Ariel A. Petruk^{§¶1}, Martín Hugo^{‡1}, Dolores Piñeyro^{¶||}, Verónica Demicheli^{‡1}, Diego M. Moreno^{**}, Analía Lima^{‡‡}, Carlos Batthyány^{‡‡‡}, Rosario Durán^{‡‡}, Carlos Robello^{¶||}, Marcelo A. Martí[§], Nicole Larrieux^{§§}, Alejandro Buschiazzo^{§§¶¶1}, Madia Trujillo[‡], Rafael Radi^{‡2,3}, and Lucía Piacenza^{‡2,4}

From the [‡]Departamento de Bioquímica and Center for Free Radical and Biomedical Research, Facultad de Medicina, Universidad de la República, Montevideo 11800, Uruguay, the ^{||}Unit of Molecular Biology, ^{§§}Unit of Protein Crystallography, and ^{‡‡}Unit of Analytical Biochemistry and Proteomics, Institut Pasteur de Montevideo/IIBCE, Mataojo 2020, Montevideo 11400, Uruguay, ^{¶¶}Institut Pasteur, Department of Structural Biology and Chemistry, 25 rue du Dr. Roux, Paris 75015, France, the [§]Facultad de Ciencias Exactas y Naturales and Departamento de Química Biológica Universidad de Buenos Aires, INQUIMAE-CONICET, Pab 2 Ciudad Universitaria, Buenos Aires, Argentina, [¶]Instituto de Química del Noroeste Argentino, CONICET-UNT, Ayacucho 471, S.M. de Tucumán, Tucumán T4000CAN, Argentina, and the ^{**}Instituto de Química Rosario (QUIR-CONICET), Facultad de Ciencias Bioquímicas y Farmacéuticas, Universidad Nacional de Rosario, Suipacha 531, Rosario S2002LRK, Argentina

Background: Superoxide dismutases are inactivated by peroxynitrite.

Results: *T. cruzi* cytosolic Fe-SODB is highly resistant toward peroxynitrite-mediated tyrosine nitration and inactivation as compared with mitochondrial Fe-SODA.

Conclusion: Intramolecular electron transfer in Fe-SODB from Cys⁸³ to critical Tyr³⁵ prevents enzyme nitration and inactivation.

Significance: Disparate susceptibilities of Fe-SODs to peroxynitrite can influence parasite virulence during *T. cruzi* infection of mammalian cells.

Trypanosoma cruzi, the causative agent of Chagas disease, contains exclusively iron-dependent superoxide dismutases (Fe-SODs) located in different subcellular compartments. Peroxynitrite, a key cytotoxic and oxidizing effector biomolecule, reacted with *T. cruzi* mitochondrial (Fe-SODA) and cytosolic (Fe-SODB) SODs with second order rate constants of $4.6 \pm 0.2 \times 10^4 \text{ M}^{-1} \text{ s}^{-1}$ and $4.3 \pm 0.4 \times 10^4 \text{ M}^{-1} \text{ s}^{-1}$ at pH 7.4 and 37 °C, respectively. Both isoforms are dose-dependently nitrated and inactivated by peroxynitrite. Susceptibility of *T. cruzi* Fe-SODA toward peroxynitrite was similar to that reported previously for *Escherichia coli* Mn- and Fe-SODs and mammalian Mn-SOD, whereas Fe-SODB was exceptionally resistant to oxidant-mediated inactivation. We report mass spectrometry analysis indicating that peroxynitrite-mediated inactivation of *T. cruzi* Fe-SODs is due to the site-specific nitration of the critical and universally conserved Tyr³⁵. Searching for structural differences, the crystal structure of Fe-SODA was

solved at 2.2 Å resolution. Structural analysis comparing both Fe-SOD isoforms reveals differences in key cysteines and tryptophan residues. Thiol alkylation of Fe-SODB cysteines made the enzyme more susceptible to peroxynitrite. In particular, Cys⁸³ mutation (C83S, absent in Fe-SODA) increased the Fe-SODB sensitivity toward peroxynitrite. Molecular dynamics, electron paramagnetic resonance, and immunospin trapping analysis revealed that Cys⁸³ present in Fe-SODB acts as an electron donor that repairs Tyr³⁵ radical via intramolecular electron transfer, preventing peroxynitrite-dependent nitration and consequent inactivation of Fe-SODB. Parasites exposed to exogenous or endogenous sources of peroxynitrite resulted in nitration and inactivation of Fe-SODA but not Fe-SODB, suggesting that these enzymes play distinctive biological roles during parasite infection of mammalian cells.

Superoxide dismutases (SODs⁵; EC 1.15.1.1) are metalloenzymes essential for all living aerobic organisms that catalyze the detoxification of superoxide radicals (O₂⁻) to oxygen (O₂) and hydrogen peroxide (H₂O₂). They are subdivided into three structurally distinct families, depending on the metal of the active site:

* This work was supported, in whole or in part, by National Institutes of Health Grant 1R01AI095173. This work was also supported by a grant from the Universidad de la República (CSIC, Uruguay) (to R.R.) and by PEDECIBA (Programa de Desarrollo de Ciencias Básicas, Uruguay) and CeBEM (Centro de Biología Estructural del Mercosur).

¹ Supported by a fellowship from the Agencia Nacional de Investigación e Innovación (ANII, Uruguay).

² Supported by Biriden, ASM, and Ridaline through Fundación Manuel Pérez, Facultad de Medicina, Universidad de la República.

³ To whom correspondence may be addressed. E-mail: rradi@fmed.edu.uy.

⁴ To whom correspondence may be addressed. E-mail: lpiacenza@fmed.edu.uy.

⁵ The abbreviations used are: SOD, superoxide dismutase; NEM, *N*-ethylmaleimide; DTNB, 5,5'-dithiobis-(2-nitrobenzoic acid); PBN, α -phenyl *N*-tertiary-butyl nitron; NOC-12, 1-hydroxy-2-oxo-3-(*N*-ethyl-2-aminoethyl)-3-ethyl-1-triazene; DMPO, 5,5-dimethyl-1-pyrroline-*N*-oxide; IPG, immobilized pH gradient; AA, antimycin A; IET, intramolecular electron transfer.

(i) copper/zinc (Cu/Zn-SODs) existing in eukaryotes and bacteria; (ii) iron/manganese (Fe/Mn-SODs) found in bacteria and several higher plants; and (iii) Ni-SODs present in bacteria of the *Streptomyces* species (1). Fe- and Mn-SODs exhibit a high degree of sequence and structure similarity, strongly suggesting that these enzymes originate from a common ancestor (2).

Trypanosomatids of the genus *Leishmania*, *Trypanosoma brucei*, and *Trypanosoma cruzi* are primitive eukaryotes containing exclusively Fe-SODs isoforms. For *T. cruzi*, the causative agent of Chagas disease, two SOD genes have been cloned and characterized: mitochondrial Fe-SODA and cytosolic Fe-SODB (3, 4). Chagas disease remains a major public health concern in Latin America, with an estimated total of 11 million people infected and 28 million at risk, according to the World Health Organization. Moreover, the disease is spreading worldwide as a result of migration (mammalian host and insect vectors), HIV co-infection, blood transfusion, and organ transplantation, as evidenced by the fact that 1 of every 4700 blood donors test positive for *T. cruzi*. The United States Centers for Disease Control estimates that there are 300,000 infected persons living in the United States as of 2010. The availability of drugs to treat the disease is currently minimal, and there is an urgent need for new drugs, which requires the proper identification of critical molecular targets and metabolic pathways that may differ from the mammalian host cells (5, 6). In this context, the antioxidant armamentarium of *T. cruzi* has been recently recognized to participate in parasite virulence (7); therefore, it is important to obtain a more detailed understanding of the interplay between oxidants formed during *T. cruzi* invasion to mammalian host cells and the parasite antioxidant enzyme network and how these processes influence the outcome of the infection.

During the acute infection, resident macrophages, at the site of parasite invasion, are among the first professional phagocytes to be invaded by *T. cruzi* (8, 9). To establish the infection, the invading *T. cruzi* needs to survive the highly oxidizing environment of the macrophage phagosome before escaping to the "safer" cytoplasmic milieu (10). The macrophage NADPH oxidase is activated during *T. cruzi* phagocytosis, resulting in a sustained (60–90-min) O_2^- production toward the internalized parasite (10). Macrophage-derived O_2^- is not particularly toxic *per se* to *T. cruzi*, in part because of its limited diffusion inside the parasite and also because of the ubiquitous presence of Fe-SODs, which promote its fast dismutation to hydrogen peroxide (H_2O_2). Alternatively, in immunostimulated macrophages, O_2^- reacts with nitric oxide (*NO , derived from the inducible nitric-oxide synthase) at diffusion-controlled rates ($k = 1 \times 10^{10} M^{-1} s^{-1}$) to yield peroxynitrite, a strong oxidant and potent cytotoxic effector molecule against *T. cruzi* (10). In nonphagocytic cells, such as cardiomyocytes, mammalian cell-derived *NO may exert cytotoxic actions on *T. cruzi* associated with an increase in O_2^- generation by the respiratory chain and peroxynitrite formation in mitochondria (11). Enhanced mitochondrial O_2^- steady-state levels trigger *T. cruzi* programmed cell death (12). Importantly, Fe-SODA overexpressers are more resistant to apoptotic stimuli, revealing the participation of the enzyme in the fine tuning of the death signaling process (12).

The efficient removal of O_2^- by Fe-SODs can attenuate peroxynitrite formation in different *T. cruzi* subcellular compartments. However, the *NO and O_2^- reaction occurs in biological systems despite the presence of SODs because it can outcompete the enzyme-catalyzed O_2^- dismutation (13). Moreover, in the case of mammalian Mn-SOD, it is well established that it can be efficiently inactivated by peroxynitrite (14), which increases O_2^- levels, and subsequently peroxynitrite, creating a hazardous positive feedback loop that can impair mitochondrial energy metabolism (15) and the signaling of programmed cell death (16). In this scenario, it is reasonable to hypothesize that the contents of parasite Fe-SODs and the fluxes of O_2^- , *NO , and peroxynitrite may be important determinants in parasite survival or death during the infection process.

The mechanism of the peroxynitrite-dependent inactivation of mammalian Mn-SOD has been extensively studied and involves the preferential nitration of Tyr³⁴, located 5 Å from the manganese ion of the active site (14, 17–20). This site-specific nitration has been ascribed to a kinetically favored reaction of peroxynitrite with the manganese ion, leading to the formation of oxidizing and nitrating species at the active site (18, 21). Due to the high degree of structural homology that Mn- and Fe-SODs share (2), a similar mechanism for peroxynitrite-dependent *T. cruzi* Fe-SODs enzyme inactivation may be expected. In this work, we have studied the reaction of peroxynitrite with the purified cytosolic and mitochondrial isoforms of *T. cruzi* Fe-SODs. The results obtained revealed outstanding differences between both *T. cruzi* SODs isoforms in terms of their susceptibility to peroxynitrite-mediated nitration and inactivation, with the cytosolic Fe-SODB being extremely resistant to oxidant treatment. The biochemical basis for the observed disparate oxidant susceptibility between both *T. cruzi* Fe-SODs was analyzed at the structural and molecular levels. Moreover, the occurrence of these biochemical events under cellular nitroxidative stress conditions was unambiguously established in *T. cruzi* Fe-SOD overexpressers, confirming the preferential nitration and inactivation of Fe-SODA in living parasites.

EXPERIMENTAL PROCEDURES

Chemicals

N-Ethylmaleimide (NEM), diethylenetriaminepentaacetic acid, 5,5'-dithiobis-(2-nitrobenzoic acid) (DTNB), manganese dioxide, Dulbecco's modified Eagle's medium (DMEM), lipopolysaccharide (LPS), Geneticin (G418), *L*-cysteine-methyl ester, 4-(2-pyridylazo)-resorcinol, and α -phenyl *N*-tertiary-butyl nitron (PBN) were from Sigma. The nitric oxide donor 1-hydroxy-2-oxo-3-(*N*-ethyl-2-aminoethyl)-3-ethyl-1-triazene (NOC-12) was from Dojindo. Murine recombinant IFN- γ was from Calbiochem. Lab-Tek tissue culture chamber slides were from Nunc. All other chemicals were of reagent grade. Peroxynitrite was synthesized in a quenched flow reactor from sodium nitrite and hydrogen peroxide (H_2O_2) under acidic conditions and quantitated as described previously; excess H_2O_2 was removed by treatment with MnO_2 , and NO_2^- contamination was always <20% (22). Peroxynitrite concentration was determined spectrophotometrically at 302 nm ($\epsilon_{302\text{ nm}} = 1670 M^{-1}$

Peroxynitrite-mediated Inactivation of *T. cruzi* Fe-SODs

cm^{-1}) (23). The spin trap 5,5-dimethyl-1-pyrroline-*N*-oxide (DMPO) and the anti-DMPO rabbit antiserum were kindly provided by Dr. Ronald Maison (NIEHS, National Institutes of Health, Bethesda, MD).

Expression, Purification, and Site-directed Mutagenesis of *T. cruzi* Cytosolic Fe-SODB and Mitochondrial Fe-SODA

Parasite SOD genes were amplified from *T. cruzi* genomic DNA (CL-Brener strain) using the following primers: Fe-SODA, 5'-GGATCCGCCCGGCCGAGTTGCCCAA-3' (forward) and 5'-GGAAGCTTTATTTTATTGCCTGCGCATG-3' (reverse); Fe-SODB, 5'-GGGGATCCATGGTCTTCAGCATTCCTCC-3' (forward) and 5'-GGAAGCTTCGTGGGTCAAAGTTGTCG-3' (reverse) (restriction sites for BamHI and HindIII, respectively, are underlined). The purified PCR product (BIORON gel extraction kit) was ligated into the pGEM-T Easy vector (Promega) and transformed into electrocompetent *Escherichia coli* XL1 blue cells. The amplified *T. cruzi* Fe-SODA (without mitochondrial signal peptide) and Fe-SODB genes were cloned into the pQE-30 vector (Qiagen) between BamHI and HindIII. pQE30-Fe-SODs in *E. coli* M15 (pREP4) cells were grown at 37 °C in LB broth containing ampicillin (100 $\mu\text{g}/\text{ml}$) and kanamycin (50 $\mu\text{g}/\text{ml}$). Expression of recombinant Fe-SODs was induced with isopropyl- β -D-thiogalactopyranoside (0.8 mM) when the culture reached $A_{600} = 0.6$, and the temperature was lowered to 22 °C for overnight protein expression. The purification was performed in a 5-ml HiTrap affinity column (Amersham Biosciences) charged with Ni^{2+} and equilibrated with binding buffer (50 mM sodium phosphate, pH 7.6, containing imidazole (10 mM) and NaCl (500 mM) at a flow rate of 3 ml/min. Fe-SODs were eluted with a linear imidazole (10–500 mM) gradient in sodium phosphate (50 mM, pH 7.6) containing NaCl (500 mM). Imidazole was removed by buffer exchange with sodium phosphate buffer (50 mM, pH 7.4) using HiTrap desalting columns (Amersham Biosciences). Purity of *T. cruzi* Fe-SOD preparations was evaluated by SDS-PAGE, and protein concentration was measured by the Bradford method (24). Molecular weight of the purified enzymes was evaluated by gel filtration chromatography in a SuperdexTM-200 column (GE Healthcare) calibrated with the following protein standards: 13,700, 29,000, 43,000, and 75,000 Da (GE Healthcare). Iron content was measured by the 4-pyridylazo-resorcinol method (25).

Site-directed mutagenesis of *T. cruzi* Fe-SODB (C159S) was performed by PCR from plasmidic DNA (pQE30-SODB) with *Pfu* Turbo DNA polymerase 1.25 units (Fermentas) using the following primers (0.4 μM): forward, 5'-ACTTGAAGCCTCTCCT-TACAAGCGATGTATGGGAG-3'; reverse, 5'-CTCCCATACATCGCTTGTAAGGAGAGGCTTCAAGT-3'. The PCR was performed with an annealing temperature of 55 °C (16 cycles) and extension temperature of 68 °C (8 min). Following PCR, the mutated DNA was selected with DpnI (Biolabs), which degrades parental methylated DNA. Sequence fidelity was confirmed by DNA sequencing (Institut Pasteur, Montevideo, Uruguay). Fe-SODB C83S and N187D/K189E mutants were purchased from GenScript. Proteins were expressed and purified as described above.

Determination of *T. cruzi* Fe-SOD Rate Constants with O_2^-

The O_2^- dismutase activity of the purified *T. cruzi* recombinant Fe-SODA and Fe-SODB was measured by the decrease in the rate of superoxide-dependent cytochrome *c* reduction at 550 nm using xanthine/xanthine oxidase as a superoxide source (26). The rate constants of *T. cruzi* Fe-SODA and Fe-SODB were determined by the kinetic competition method described previously. Xanthine-oxidase (6 milliunits) and xanthine (50 μM) were used for the generation of O_2^- fluxes. The reduction of ferricytochrome *c* (20 μM) was monitored at 550 nm at 37 °C in phosphate buffer 50 mM, pH 7.8, using a 1-ml cuvette in the absence and presence of Fe-SODA or Fe-SODB (0–40 nM). The velocity of cytochrome *c* reduction in the absence (V_0) and presence of Fe-SOD (V_{SOD}) was employed to calculate an inhibition fraction ($\text{IF} = 1 - (V_0 - V_{\text{SOD}})/V_0$). Utilizing the reported bimolecular rate constant for the reaction of O_2^- with ferricytochrome *c* at pH 7.8 ($2.6 \pm 0.1 \times 10^5 \text{ M}^{-1} \text{ s}^{-1}$), the rate constants were calculated as $k_{\text{SOD}} = k_{\text{cyt}} ([\text{cyt}]/[\text{FeSOD}]_{50})$. $[\text{FeSOD}]_{50}$ (the concentration of SOD that caused an inhibition fraction of 0.5) was obtained from the fitting of experimental data to a rectangular hyperbolic curve (27).

Kinetics Studies of *T. cruzi* Fe-SOD Reactions with Peroxynitrite

The kinetics of peroxynitrite (10 and 17 μM for Fe-SODA and Fe-SODB, respectively) decomposition was monitored at 302 nm ($\epsilon_{302} = 1670 \text{ M}^{-1} \text{ cm}^{-1}$) in the presence or absence of control and NEM-treated Fe-SODA and Fe-SODB (0–15 μM) in a stopped-flow spectrophotometer (SX20, Applied Photophysics) with a mixing time of <2 ms. An initial rate approach was used to analyze the data (28); the first 0–0.15 s of peroxynitrite decomposition was fitted to a linear plot, and initial rates were calculated by dividing the slope of the absorbance time course by the peroxynitrite molar extinction coefficient at 302 nm and multiplying by a factor of 1.25 to account for the 20% fraction of peroxynitrite that is not deprotonated at pH 7.4 (because the absorption at 302 nm is due to the peroxynitrite anion). Second order rate constants (k_2) were calculated according to the equation, $v_0 = (k_1 + k_2 \times [\text{Fe-SOD}]_0) \times [\text{peroxynitrite}]_0$, where k_1 is the rate constant of proton-catalyzed peroxynitrite decomposition (28). Reported values are the average of at least seven separate determinations. Temperature was maintained at 37 °C, and the pH was measured at the outlet.

Measurements of Protein Thiol Content and Thiol Alkylation

Protein thiols were quantitated using the DTNB assay (29). Protein thiols were reduced by incubation with DTT (1 mM) for 30 min at room temperature. Alkylation of *T. cruzi* Fe-SOD thiol groups by NEM was performed by incubation of Fe-SODA or Fe-SODB (200 μM) with NEM (10 mM) for 2 h in phosphate buffer (50 mM, pH 7.4) at 4 °C. Excess DTT and NEM were removed immediately after incubation using HiTrap desalting columns (Amersham Biosciences) as described previously (30).

Peroxynitrite Treatment of *T. cruzi* Fe-SODs

Peroxynitrite (0–2000 μM) was added as a single dose under vortex to the purified enzymes (8 μM) in sodium phosphate buffer (200 mM, pH 7.4), and activity was measured as described

above. Peroxynitrite addition was done to control or NEM-treated enzymes in the presence or absence of GSH (10 mM), uric acid (100 μ M), L-cysteine methyl ester (8 μ M), bicarbonate (25 mM), PBN (50 mM), and DMPO (100 mM). Peroxynitrite addition was also performed at different pH values (5.8–8.0), and *T. cruzi* Fe-SODs activity was measured as described above.

Western Blotting, Protein Nitrotyrosine, and Immunospin Trapping Analysis

After treatment, proteins were subjected to 15% SDS-PAGE, transferred to nitrocellulose membranes, and blocked in phosphate-buffered saline (PBS; 50 mM, pH 7.4) containing dry milk (5% w/v) for 1 h. Membranes were then probed with either rabbit polyclonal anti-nitrotyrosine antibody (1:2000 dilution raised in our laboratory (31)) or rabbit polyclonal anti-*T. cruzi* Fe-SODA or Fe-SODB (1:5000 dilution (32)) in PBS containing Tween 20 (0.1%, v/v) for 1 h. Membranes were washed and probed for 1 h with anti-rabbit-IgG (IR Dye-800- and IR Dye-680-conjugated (LI-COR Biosciences) or peroxidase-conjugated (Calbiochem), 1:15,000 dilution in PBS containing Tween 20 (0.1%, v/v)). After washing of the probed membranes, immunoreactive proteins were visualized with an infrared fluorescence detection system (Odyssey, LI-COR Biosciences) or using the Immun-StarTM chemiluminescence kit (Bio-Rad). For immune spin trapping, after exposure of *T. cruzi* Fe-SODB (50 μ M) to peroxynitrite (5–20 μ M) in the presence or absence of DMPO (100 mM), protein samples were subjected to Western blot analysis, and protein-DMPO nitron adducts were detected using a rabbit polyclonal anti-DMPO-nitron primary antibody (rabbit anti-DMPO serum, 1:2,000 dilution in PBS containing Tween 20 (0.1%, v/v) and bovine serum albumin (4%, v/v)) as described previously (33). Immunoreactive proteins were detected with the infrared system as described above.

EPR Studies

The EPR spectra were recorded at room temperature (25 °C) on a Bruker EMX EPR spectrometer. Wild type Fe-SODB or C83S single mutant (2 mM) were incubated with the spin trap PBN (50 mM) and exposed to peroxynitrite (500 μ M). Immediately after oxidant addition, samples were transferred to a 200- μ l flat cell, and the spectra were recorded within 1 min (15 spectrum acquisitions). Adducts between Fe-SODs and PBN were digested with Pronase (20 mg/ml) for 10 min, and spectra were recorded as above.

Peptide Mapping Analysis of Peroxynitrite-treated *T. cruzi* Fe-SODs

T. cruzi Fe-SODs (8 μ M) were treated with peroxynitrite (0–300 μ M) in potassium phosphate buffer (200 mM, pH 7.4) at 25 °C in the presence or absence of DMPO (100 mM). Protein samples were separated by one- or two-dimensional gel electrophoresis. Commercially available IPG strips (7 cm, linear 3–10, GE Healthcare) were used for the first dimensional separation. Enzymes were purified and concentrated with 2-D Clean-up (GE Healthcare) and dissolved in 125 μ l of rehydration solution (7 M urea, 2 M thiourea, 2% (w/v) CHAPS, 0.5% (v/v) IPG buffer 3–10 (GE Healthcare), 0.002% (w/v) bromophenol blue, and 17 mM DTT). Samples in rehydration solution

were loaded onto IPG strips by passive rehydration during 12 h at room temperature. The isoelectric focusing was done in an IPGphor unit (GE Healthcare) employing the following voltage profile: constant phase of 300 V for 30 min, linear increase to 1000 V in 30 min, linear increase to 5000 V in 80 min, and a final constant phase of 5000 V to reach a total of 2.0 kWh. Prior to running the second dimension, IPG strips were reduced for 15 min in equilibration buffer (6 M urea, 75 mM Tris-HCl, pH 8.8; 29.3% (v/v) glycerol, 2% (w/v) SDS, and 0.002% (v/v) bromophenol blue) supplemented with 10 mg/ml (DTT) and subsequently alkylated with iodoacetamide (25 mg/ml). The second dimensional separation was performed in 15% SDS-PAGE using an SE 260 minivertical gel electrophoresis unit (GE Healthcare). Gels were stained with Colloidal Coomassie Blue G-250. Images were digitized using a UMAX Power-Look 1120 scanner and LabScan version 5.0 software (GE Healthcare). Selected spots from two-dimensional gels or bands from one-dimensional gels were manually removed and in-gel digested with trypsin (sequencing grade; Promega) as described (34). Peptides were extracted from gels using aqueous acetonitrile (60%, v/v) containing trifluoroacetic acid (TFA; 0.1%, v/v) and concentrated by vacuum drying. Peptide mixtures were analyzed using a linear ion trap mass spectrometer (LTQ Velos, Thermo) coupled online with a nanoliquid chromatography system (Easy-nLC, Proxeon-Thermo) or using a MALDI-TOF/TOF mass spectrometer (4800 MALDI TOF/TOF, ABi Sciex). For the nano-LC/MS approach, peptides were separated on a reversed-phase column (Aquasil C18 100 mm, inner diameter 75 μ m, 5 μ m, PicoFRITTM column from New Objective) and eluted with a linear gradient of acetonitrile (0.1% formic acid (0–40% in 55 min) at a flow rate of 0.3 μ l/min). Electrospray voltage was 1.40 kV, and capillary temperature was 200 °C. Peptides were detected in the positive ion mode using a mass range of 300–2000, and MS/MS of the top five peaks in each segment were acquired in a data-dependent manner. Peptides were identified by searching public databases (NCBIInr, November 2012) and using the following Mascot MS/MS ion search mode parameters: peptide tolerance, 1.2 Da; MS/MS tolerance, 0.8 Da; methionine oxidation and tyrosine nitration as variable modifications. The significance limit for peptide identification was set at $p < 0.05$. MALDI TOF/TOF experiments were performed in the positive ion reflector mode, and mass spectra were externally calibrated using a mixture of peptide standards (Applied Biosystems). Peptide sequences were confirmed by MS/MS analysis of selected ions.

Nitrotyrosine Quantification

For total 3-nitrotyrosine quantification, peroxynitrite in a wide concentration range (0.05–3000 μ M) was added to Fe-SODs (8–16 μ M) in sodium phosphate buffer (200 mM, pH 8–5.8). NO₂⁻ removal from the samples after peroxynitrite treatment was carried out by two subsequent protein precipitation steps with acetonitrile (1 volume) for 40 min at 4 °C following centrifugation at 14,000 \times g for 40 min at 4 °C. Proteins were resuspended in nanopure water (500 μ l) containing the following internal standards: universal labeled tyrosine ([U-¹³C₉,¹⁵N₁]Tyr, 20 nmol); [NO₂-¹³C₆]Tyr (500 pmol); and [¹³C₆]Tyr (35). Stable isotopically labeled precursors were used as internal standards for the quantification of total protein Tyr and NO₂-Tyr ([U-¹³C₉,¹⁵N₁]Tyr and [NO₂-¹³C₆]Tyr, respec-

Peroxynitrite-mediated Inactivation of *T. cruzi* Fe-SODs

tively) together with [$^{13}\text{C}_6$]Tyr to monitor for potential artifactual generation of NO_2 -Tyr during sample processing. Proteins were hydrolyzed overnight at 116 °C in HCl (6 N) using vacuum hydrolysis tubes (Pierce). After hydrolysis, samples were evaporated, and pellet was resuspended (35) in 200 μl of formic acid (0.1%, v/v) and analyzed by LC-MS/MS (Qtrap Applied Biosystems) as described previously (36).

Crystal Structure of *T. cruzi* Mitochondrial Fe-SODA

The crystal structure of the mitochondrial superoxide dismutase from *T. cruzi* (Fe-SODA) was determined at 2.23 Å resolution in the Protein Crystallography Facility of the Institut Pasteur de Montevideo (Protein Data Bank entry 4DVH). Fe-SODA crystals were grown in a hanging drop vapor diffusion setup, using the protein at 2.33 mg/ml in 50 mM sodium phosphate, pH 7.8. Protein (1 μl) was mixed in equal parts with mother liquor (1-ml reservoir), Tris-HCl (0.1 M, pH 8.5), and PEG 4000 (30%, w/v) and incubated at 291 K. Monoclinic crystals grew in a few days, were cryoprotected with mother liquor containing 25% (v/v) glycerol, and flash-frozen in liquid N_2 until data collection. A complete data set was collected at 100 K with a copper rotating anode (Micromax-HF, Rigaku) and a Mar345DTB (Mar Research) image plate detector. Data were processed with MOSFLM (37) and Scala (38). The crystal structure was solved by molecular replacement with AMoRe (39) using the monomer of *E. coli* Fe-SOD (Protein Data Bank entry 2NYB) as a search probe. Restrained refinement was done with Buster-TNT (40) (BUSTER version 2.10.0, Global Phasing Ltd., Cambridge, UK), including a TLS model with one body per chain (one dimer in the asymmetric unit). Refinement was performed in iteration with manual model building using Coot (41). Structure validation was done with Molprobity (42).

Molecular Dynamics (MD) Simulations

Starting Structures—The crystal structure of the *T. cruzi* cytosolic wild type (WT) Fe-SODB was downloaded from the Protein Data Bank (Protein Data Bank entry 2GPC). Based on the WT structure, double mutant N187D/K189E was built *in silico* by replacing the corresponding residue side chains. Hydrogens were added using the Tleap module of the AMBER program package, considering standard protonation states for all titratable residues at physiological pH (Asp and Glu negatively charged, Lys and Arg positively charged, all of the rest neutral). Additionally, the tyrosyl radical (Tyr 35 -O \cdot) and negatively charged cysteine (Cys-S $^-$, thiolate)-containing system (tyrosyl radical-thiolate cytosolic Fe-SODB) was built by removing the corresponding phenolic and thiol hydrogens and changing the corresponding classical residue parameters (see below).

MD Simulation Parameters—Simulation of WT, mutant, and tyrosyl radical-thiolate cytosolic Fe-SODB homodimers was performed in an explicit solvent box (of $\sim 513\text{-nm}^3$ volume and containing $\sim 15,000$ water molecules) using the TIP3P water model. Parameters for all standard residues were taken from the PARM99 force field (43). Classical parameters for Tyr-O \cdot and Cys 83 -S $^-$ were taken from our previous work (44). Parameters for the Fe-SOD active site (the iron ion and its first sphere coordinating residues) were developed in the same way

as those for Mn-SOD (20). All simulations were performed using the periodic boundary conditions approximation and the particle mesh Ewald summation method with a grid spacing of 1 Å for treating long range electrostatic interactions, whereas a direct cut-off distance of 8 Å was used for direct interactions. The Shake method was used to constrain the hydrogen atoms at their equilibrium distance, allowing the use of a 2-fs time step. The Berendsen thermostat was used to keep the temperature constant at 300 K (45). All MD simulations were performed with the AMBER program package (46). The equilibration protocol for all peptides consisted of slowly heating the optimized structures from 0 to 300 K during 0.1 ns while the volume of the system was kept constant (NVT). Next, a 0.2-ns-long density equilibrium simulation was performed using an NPT ensemble. Production simulations consisted of 10-ns-long NPT MD simulations for wild type and mutant cytosolic Fe-SODB and 20-ns-long NPT MD simulation for radical-thiolate cytosolic Fe-SODB. The stability of all simulations was assessed through root mean square deviation and root mean square fluctuation analysis (data not shown).

Analysis of the Intramolecular Electron Transfer (IET) Pathway(s)

IET pathways along the protein matrix were determined using the pathways algorithm developed previously (47, 48), with a specific set of parameters developed in our group to consider the Fe-SOD active site as well as recent observations of aromatic residues acting as stepping stones in long range electron transfer reactions (49–52). The method has been used successfully in previous work from our group (44, 51, 53). Pathways were computed between Cys 83 -S $^-$ and Tyr 35 -O \cdot atoms located orbitals for 100 snapshots taken from the corresponding MD simulation. To estimate the $\text{p}K_a$ of the different Cys residues in WT and mutant cytosolic and mitochondrial Fe-SODs, the propKa $\text{p}K_a$ estimation software was used (54–57).

Parasites

T. cruzi epimastigotes (CL-Brener) were cultured at 28 °C in brain-heart infusion medium as described previously (12). *T. cruzi* CL-Brener (pTcINDEX-9E10) (Invitrogen) Fe-SODA overexpressers containing the bacteriophage T7 RNA polymerase, tetracycline (Tet) repressor genes, and the epitope (9E10) derived from the human c-Myc protein added to the C terminus of Fe-SODA were maintained as described previously in brain-heart infusion medium containing G418 and hygromycin (100 $\mu\text{g}/\text{ml}$) (12, 58). To induce Fe-SODA expression, epimastigotes were cultured in medium supplemented with tetracycline (2 $\mu\text{g}/\text{ml}$) for 3 days as described previously (12).

Nitroxidative Treatment of *T. cruzi* Epimastigotes

T. cruzi Fe-SODA overexpressers were used in order to identify, at the cellular level, peroxynitrite-dependent *T. cruzi* Fe-SOD nitroxidative modifications. For this, Fe-SOD parasites (5×10^8 cells/ml in Dulbecco's PBS, pH 7.4) were treated with the mitochondrial complex III inhibitor antimycin A (AA; 5 μM) in the presence of NOC-12 (5 mM, $t_{1/2} = 100$ min at pH 7.4), SIN-1 (5 mM), or peroxynitrite (300 μM in three subsequent additions of 100 μM) for 3 h at 28 °C under stirring (59). After

treatment, parasites were washed three times in Dulbecco's PBS and resuspended in Tris-HCl (40 mM, pH 7.4) containing urea (7 M), thiourea (2 M), CHAPS (4%, w/v), PMSF (1 mM), and DTT (1%, w/v). Two-dimensional electrophoresis was performed with commercially available IPG strips (7 cm, non-linear 3–10, GE Healthcare) for the first dimensional separation. Protein samples (390 μ g) were dissolved in rehydration solution (7 M urea, 2 M thiourea, 2% (w/v) CHAPS; 0.5% IPG buffer 3–10 (GE Healthcare), 0.002% (w/v) bromphenol blue, 17 mM DTT) and loaded onto IPG strips by passive rehydration during 12 h at room temperature. The isoelectric focusing was done in an IPGphor unit (GE Healthcare) employing the following voltage profile: linear increase to 150 V in 30 min; constant phase of 300 V for 2 h; constant phase of 500 V for 1 h; constant phase of 1000 V for 1 h; linear increase to 5000 V in 30 min; and a final constant phase of 5000 V for 6 h to reach a total of 33.6 kV-h. Prior to running the second dimension, IPG strips were incubated for 15 min, first in equilibration buffer (6 M urea, 75 mM Tris-HCl, pH 8.8, 29.3% (v/v) glycerol, 2% (w/v) SDS, 0.002% (w/v) bromphenol blue) supplemented with 10 mg/ml DTT for protein reduction and finally in equilibration buffer supplemented with 25 mg/ml iodoacetamide for protein thiol alkylation. The second dimensional separation was performed in 15% SDS-PAGE using an SE 260 minivertical gel electrophoresis unit (GE Healthcare). Proteins were transferred to nitrocellulose membranes (40 mA, overnight) and blocked with 5% milk in PBS for 1 h. Membranes were then probed with either rabbit polyclonal anti-*T. cruzi* Fe-SODA or Fe-SODB (1:2000 dilution), and immunoreactive proteins were visualized as described above.

Immunoprecipitation of *T. cruzi* Fe-SODA

T. cruzi Fe-SODA overexpressers were incubated under different nitroxidative stress conditions described above. After treatment, parasites (1×10^9) were washed three times in Dulbecco's PBS and lysed in 250 μ l of Tris-HCl (20 mM, pH 7.5) containing 150 mM NaCl, 1 mM EGTA, 1% Nonidet P-40, 1% sodium deoxycholate, and protease inhibitors (Sigma). Following incubation for 15 min in ice, samples were centrifuged at 4 °C and $13,000 \times g$, and supernatants were incubated under orbital shaking at 4 °C in the presence of monoclonal anti-c-Myc antibody (30 μ g; Santa Cruz Biotechnology, Inc.) and Protein A/G Plus-agarose (20 μ l; Santa Cruz Biotechnology). After incubation, samples were centrifuged at $800 \times g$, and agarose beads were washed four times in lysis buffer. Proteins bound to agarose were released by incubating the beads with 50 μ l of Laemmli sample buffer (with 5% (v/v) β -mercaptoethanol) for 5 min at 100 °C. Proteins were separated on 15% SDS-polyacrylamide gels, transferred to nitrocellulose, and probed against anti-c-Myc (9E10) and anti-NO₂-Tyr antibodies. Immunoprecipitated proteins were developed as above using the anti-mouse IRE-680 (for Fe-SODA protein) and anti-rabbit IRE-800 (for 3-nitrotyrosine-containing proteins).

Data Analysis

All data are given as means \pm S.D. unless otherwise noted, and $p < 0.05$ was considered significant. Means were compared using Student's *t* test.

RESULTS

Purification and Characterization of Fe-SODA and Fe-SODB—The recombinant *T. cruzi* Fe-SODA and Fe-SODB containing one atom of iron per monomer were purified to homogeneity as active enzymes homodimers as established by SDS-gel electrophoresis and gel filtration chromatography analysis. The apparent monomer molecular mass was 23 and 22.6 kDa for Fe-SODA and Fe-SODB, respectively (Fig. 1, A and B), consistent with the predicted values according to their primary structures. All of the enzyme preparations used in this study, including the mutants generated, were of high purity (>99%) with specific activities of 2647 and 3551 units/mg for Fe-SODA and Fe-SODB, respectively. These specific activities compare well with previously reported *T. brucei* Fe-SODs (60).

Determination of the Rate Constant with O₂⁻ and Kinetics of the Reaction of *T. cruzi* Fe-SODs with Peroxynitrite—A competition kinetic approach was used to determine the second order rate constant of the reaction of *T. cruzi* Fe-SODs with O₂⁻, and it was found to be $4.5 \pm 1.8 \times 10^8 \text{ M}^{-1} \text{ s}^{-1}$ for Fe-SODA and $7.6 \pm 1.5 \times 10^8 \text{ M}^{-1} \text{ s}^{-1}$ for Fe-SODB in 50 mM sodium phosphate, pH 7.8 (ionic strength (μ) = 0.14), in agreement with values obtained for other iron-containing SODs (Fig. 1C and Table 1) (61).

The rate constant for peroxynitrite reaction with *T. cruzi* Fe-SODs was measured following the decay of peroxynitrite at increasing concentrations of enzyme (0–15 μ M), as described previously (18). A linear correlation was obtained after plotting the initial velocity of peroxynitrite decomposition (v_0) (Fig. 2, inset) as a function of Fe-SOD concentrations (Fig. 2), with the *y* axis intercept reflecting the proton-catalyzed decomposition of peroxynitrite (as described under “Experimental Procedures”). By dividing the slope of the plot over peroxynitrite concentration, the second order rate constant was determined as $4.6 \pm 0.2 \times 10^4 \text{ M}^{-1} \text{ s}^{-1}$ for Fe-SODA and $4.3 \pm 0.4 \times 10^4 \text{ M}^{-1} \text{ s}^{-1}$ for Fe-SODB per monomer at pH 7.4 and 37 °C, in agreement with that obtained for other SODs (Table 1) (18, 62, 63). When the rate constant was determined in the presence of Fe-SOD in which the solvent-accessible cysteines were blocked by NEM alkylation, the same value was obtained (Table 1), indicating a negligible contribution of cysteine residues ($k_{\text{ONOO}^-} = 6 \times 10^3 \text{ M}^{-1} \text{ s}^{-1}$ for free cysteine at pH 7.4 and 37 °C) to the global rate constant observed. Because the reactivity of cysteine toward peroxynitrite is typically the largest among all amino acids (28), the data support the existence of a fast direct reaction of peroxynitrite with the iron atom of the Fe-SODs.

Peroxynitrite-dependent Inactivation and Nitration of *T. cruzi* Fe-SODs—Peroxynitrite addition (0–1200 μ M) to purified Fe-SODA and Fe-SODB (8 μ M) at pH 7.4 led to a dose-dependent inhibition of the superoxide dismutase activity although with quite disparate susceptibilities (Fig. 3A). Indeed, Fe-SODB was largely resistant to peroxynitrite-mediated inactivation, in contrast with the highly sensitive Fe-SODA, an unexpected result taking into account the structural similarities between both isoforms (3, 4). Enzyme inactivation was associ-

Peroxynitrite-mediated Inactivation of *T. cruzi* Fe-SODs

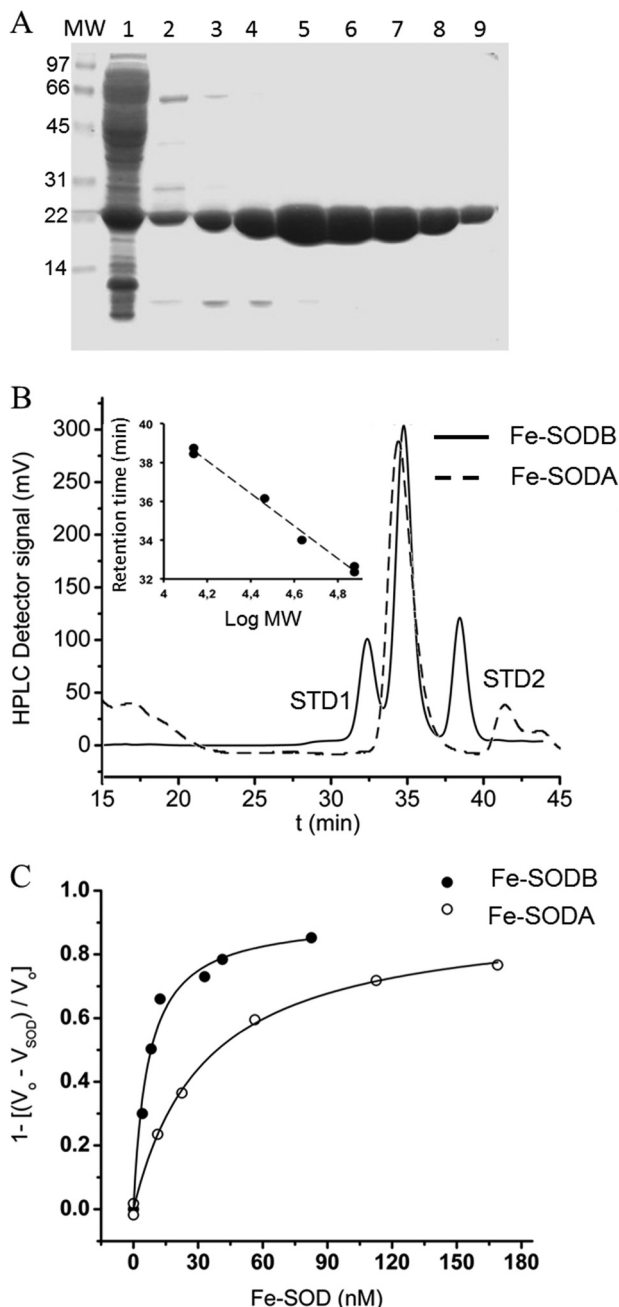


FIGURE 1. Purification of recombinant *T. cruzi* Fe-SODs and rate constants with O_2^- . A, SDS-gel electrophoresis (15% (w/v) under reducing conditions) of the eluted fractions from the Ni^{2+} affinity chromatography of Fe-SODA purification. Lane 1, soluble extract after isopropyl- β -D-thiogalactopyranoside (0.8 mM) induction; lanes 2–9, fractions eluted from the Ni^{2+} affinity chromatography using a linear imidazole gradient (10–500 mM). B, Fe-SODA pure fractions (lanes 5–9) and fractions from Fe-SODB purification were pooled and analyzed by gel filtration chromatography in Superdex 200 (solid line, Fe-SODB; dashed line, Fe-SODA). Inset, calibration of the Superdex S200 gel filtration column with molecular mass standards (13,000–75,000 Da). C, rate constants were determined by competition kinetics method. O_2^- -dependent reduction of ferricytochrome *c* (20 μ M) was monitored at 550 nm at 37 °C in the absence and presence of *T. cruzi* Fe-SODA or Fe-SODB. Rate constants were calculated as described under “Experimental Procedures” at pH 7.8 and 37 °C. Inhibition fraction ($1 - (V_0 - V_{SOD})/V_0$) was plotted as a function of Fe-SOD concentrations and fitted to a rectangular hyperbolic function in order to calculate $[Fe-SOD]_{50}$.

ated to protein tyrosine nitration, with the higher nitration yields in Fe-SODA correlating well with the level of inactivation observed (Fig. 3B).

TABLE 1

T. cruzi Fe-SOD rate constants with O_2^- and peroxynitrite

Rate constants with O_2^- were determined by the kinetic competition method as described in the legend to Fig. 1 at pH 7.8 and 37 °C. Rate constants with $ONOO^-$ were measured by an initial rate approach. $ONOO^-$ decomposition was measured at 302 nm, pH 7.4, and 37 °C as described in the legend to Fig. 2. ND, not determined.

Enzyme preparation	<i>k</i>	
	O_2^-	$ONOO^-$
	$M^{-1} s^{-1}$	
Fe-SODA	$4.5 \pm 1.8 \times 10^8$	$4.6 \pm 0.2 \times 10^4$
Fe-SODB	$7.6 \pm 1.5 \times 10^8$	$4.3 \pm 0.4 \times 10^4$
NEM-treated Fe-SODB	ND	$4.3 \pm 0.2 \times 10^4$

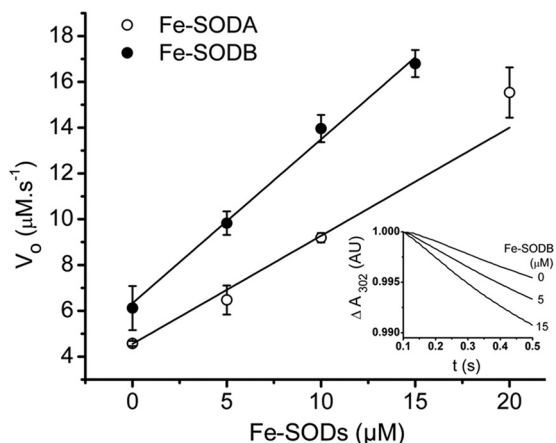


FIGURE 2. *T. cruzi* Fe-SODs rate constants with peroxynitrite. The kinetics of peroxynitrite decomposition (10 and 17 μ M peroxynitrite for Fe-SODA and Fe-SODB, respectively) was monitored at 302 nm at pH 7.4 and 37 °C in the presence of Fe-SOD (0–15 μ M) in a stopped-flow spectrophotometer. An initial rate approach (first 0–0.15 s) was used to analyze the data as described under “Experimental Procedures.” Reported values are the average of at least seven separate determinations. Inset, peroxynitrite ($ONOO^-$) decomposition in the presence of Fe-SODB (0, 5, and 15 μ M) measured at pH 7.4 and 37 °C using a stopped-flow spectrophotometer. AU, absorbance units. Error bars, S.D.

Fe-SODA and Fe-SODB B contain seven and nine tyrosine residues respectively, some of which are solvent-exposed and others of which are buried in the protein structure. Notably, Tyr³⁵ is part of the active site and the closest to the iron metal centers. Thus, in principle, tyrosine nitration could affect non-critical tyrosines as well as Tyr³⁵, with oxidative modification of the latter being responsible for enzyme inactivation. Under the experimental conditions of Fig. 3, in which biologically relevant micromolar concentrations of enzyme were used, there are two possible mechanisms by which peroxynitrite can generate nitrating intermediates to mediate Fe-SOD tyrosine nitration (64, 65): (i) the proton-catalyzed homolysis of peroxynitrous acid ($ONOOH$, $pK_a = 6.8$) to yield nitrogen dioxide ($\cdot NO_2$) and hydroxyl radical ($\cdot OH$) or (ii) the reaction of peroxynitrite anion with the iron center to yield the oxo-Fe complex and $\cdot NO_2$. To define which of the nitration mechanisms was better coupled to enzyme inactivation, we performed peroxynitrite exposures at different pH values and in the presence of CO_2 (Fig. 4), as in previous reports (66). Treatment of *T. cruzi* Fe-SODA with peroxynitrite (150 μ M) at acidic pH values (where most peroxynitrite decays via homolysis) led to mild enzyme inactivation, whereas protein nitration was high; on the contrary, at basic pH values, enzyme inactivation was more pronounced, but the yields of protein nitration were less (Fig. 4, A and B). Thus,

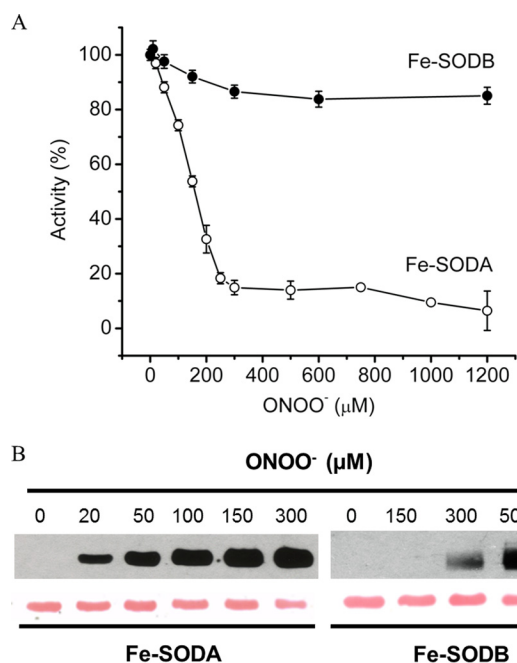


FIGURE 3. Peroxynitrite-mediated inactivation and nitration of *T. cruzi* Fe-SODA and Fe-SODB. *A*, inactivation of Fe-SODs. Peroxynitrite (ONOO^- , 0–1200 μM) was added to the purified enzymes (8 μM) at pH 7.4, and residual Fe-SOD activity was measured. Activity is expressed as a percentage relative to the control enzyme incubated in the absence of peroxynitrite (100% activity). *B*, nitration of Fe-SODs. Immunochemical detection of protein 3-nitrotyrosine (black) was performed after peroxynitrite (0–2000 μM) exposure to either Fe-SODA or Fe-SODB (8 μM) using the Immun-StarTM chemiluminescence kit. Fe-SOD loading was evaluated by Ponceau-S protein staining (pink). Error bars, S.E.

overall, these data indicate that the reactive species leading to enzyme inactivation is peroxynitrite anion via its reaction with the metal center and the site-specific nitration of active site tyrosine (see below). In support of this contention, the presence of bicarbonate (25 mM, 1.3 mM CO_2) protected Fe-SODA from peroxynitrite-mediated inactivation (Fig. 4C), as was previously seen for *E. coli* Mn-SOD (18). The reaction of peroxynitrite anion (ONOO^-) with CO_2 ($k = 3 \times 10^4 \text{ M}^{-1} \text{ s}^{-1}$ at pH 7.4 and 37 °C) yields the nitrosoperoxydicarboxylate adduct (ONOOCO_2^-) that rapidly ($<1 \mu\text{s}$) decomposes by homolysis, resulting in the generation of $\cdot\text{NO}_2$ and $\cdot\text{CO}_3^-$ radicals (67, 68). Thus, CO_2 competes with the metal of Fe-SOD for ONOO^- , yielding the secondary derived radicals that may react with solvent-accessible non-critical protein tyrosine residues without causing enzyme inactivation (19, 69, 70).

Glutathione (10 mM) known to react with peroxynitrite ($k = 1.35 \times 10^3 \text{ M}^{-1} \text{ s}^{-1}$ (71)) and $\cdot\text{NO}_2$ (72) and uric acid (100 μM), a known $\cdot\text{OH}$ and $\cdot\text{NO}_2$ scavenger ($k = 7.2 \times 10^9$ and $1.9 \times 10^7 \text{ M}^{-1} \text{ s}^{-1}$, respectively) (73, 74)) fully protected Fe-SODA from enzyme inactivation and nitration (not shown).

Peroxynitrite-dependent Inactivation of *T. cruzi* Fe-SOD by the Selective Nitration of Tyr³⁵—In order to confirm the preferential nitration of Tyr³⁵ after peroxynitrite treatment (0–300 μM) of *T. cruzi* Fe-SODs (8 μM), control and treated enzymes were separated by two-dimensional gel electrophoresis, and protein spots were analyzed by nano-LC-nano-SI-MS. One major spot for both Fe-SODA and Fe-SODB and other minor ones were identified in the native enzymes, indicating post-

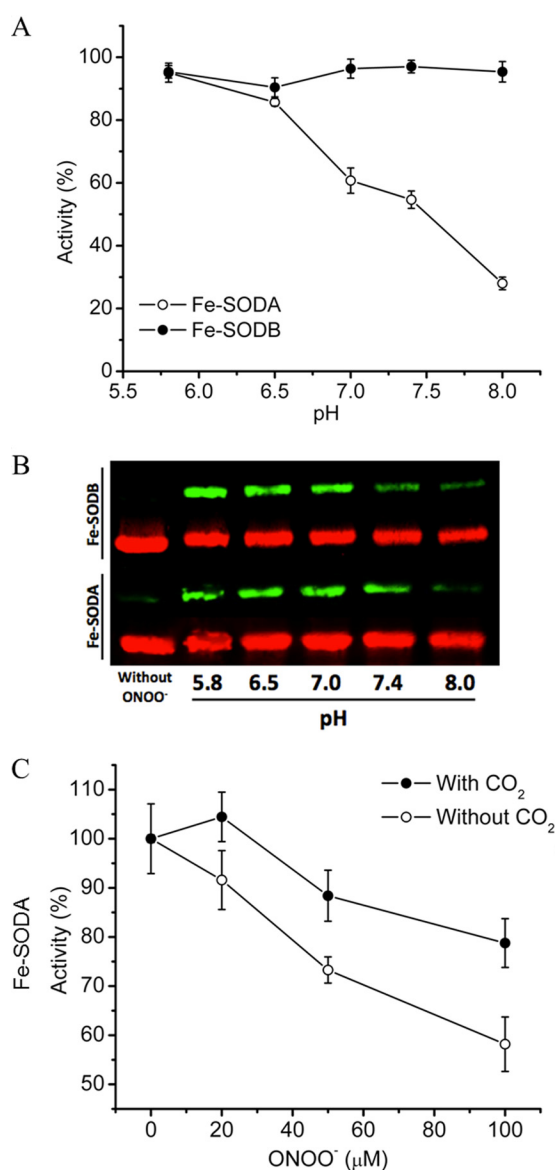


FIGURE 4. Effects of pH and CO_2 on the peroxynitrite-dependent inactivation of *T. cruzi* Fe-SODs. *A*, pH-dependent peroxynitrite-mediated inactivation. Peroxynitrite (150 μM) was added to Fe-SODA (empty circles) and Fe-SODB (filled circles) (8 μM) in sodium phosphate buffer (100 mM) at different pH values (5.5–8.0), and residual Fe-SOD activity was measured. Activity is expressed relative to the native enzyme incubated in the absence of peroxynitrite (100% activity) at the indicated pH values. *B*, pH-dependent peroxynitrite-mediated nitration. Immunochemical detection of 3-nitrotyrosine was performed after peroxynitrite (150 μM) exposure to either Fe-SODA or Fe-SODB (8 μM) in sodium phosphate buffer (100 mM) at different pH values using specific anti- NO_2 -Tyr antibodies (green). Equal loading of *T. cruzi* Fe-SOD samples were evaluated by specific Fe-SODA and Fe-SODB antibodies (red). *C*, effect of CO_2 in the peroxynitrite reaction with Fe-SODA. Peroxynitrite (0–100 μM) was added to Fe-SODA (8 μM) in sodium phosphate buffer 100 mM, pH 7.4, in the presence (filled circles) or absence (empty circles) of bicarbonate (24 mM; $\text{CO}_2 = 1.3 \text{ mM}$), and residual SOD activity was measured. Activity is expressed relative to the non-treated enzyme in the presence or absence of bicarbonate. Error bars, S.E.

translational modifications that affect the protein isoelectric point. In the case of the peroxynitrite-treated Fe-SODs, the two-dimensional gels revealed the generation of several more acidic spots in both Fe-SODs with a more drastic shift in the case Fe-SODA, in agreement with its higher susceptibility to peroxynitrite (Fig. 5A). Peroxynitrite-treated proteins are

Peroxynitrite-mediated Inactivation of *T. cruzi* Fe-SODs

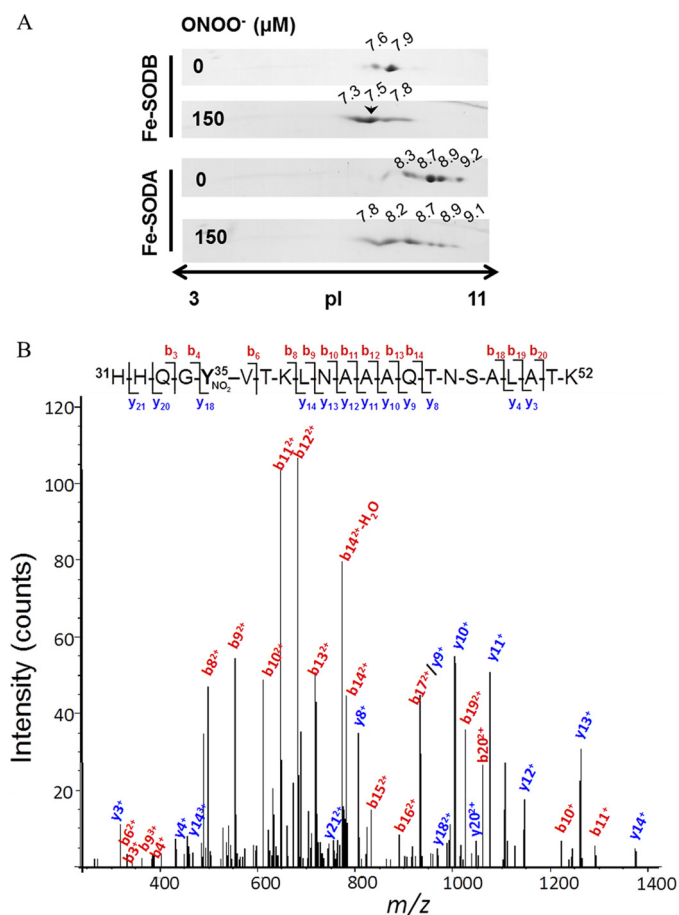


FIGURE 5. Peptide mapping of *T. cruzi* Fe-SODs after peroxynitrite treatment. A, *T. cruzi* Fe-SODs (8 μM) were treated with peroxynitrite (150 μM) in sodium phosphate buffer (0.2 M) at pH 7.4 and 25 $^{\circ}\text{C}$. Two-dimensional gel electrophoresis was performed as described under "Experimental Procedures." The arrowhead shows the selected Fe-SODB spot of pI 7.5 analyzed by mass spectrometry. B, MS/MS spectrum of triply charged ion at m/z 790.6 (MH^+ 2369.7, retention time = 30.3 min) from a tryptic digestion of peroxynitrite-treated Fe-SODB spot (pI = 7.5, indicated with an arrow in A). The major N-terminal (*b*, red-labeled) and C-terminal (*y*, blue-labeled) fragment ions that allowed the sequence 31–52 assignment that includes a nitrated tyrosine residue (mascot ion score = 61; $p < 0.05$) are shown. Inset, amino acid sequence of peptide 31–52, indicating major *b* and *y* ions detected by full-scan MS/MS.

expected to have more acidic pI values due to the change of the $\text{p}K_a$ of 3-nitrotyrosine (7.3) with respect to Tyr (10.3) (with the consequent gain of a negative charge) (21, 75), among other possible oxidative modifications. Mass spectrometry analysis of the major spot (pI = 7.5) of Fe-SODB generated after peroxynitrite treatment (150 μM) revealed the presence of only one nitrated peptide (m/z = 790) corresponding to the triple charged molecular ion, assigned to the sequence $^{31}\text{HHQGG}^{35}\text{YVTKLNAQAQTNSALATK}^{52}$, which contained Tyr³⁵ (Fig. 5B), revealing the preferential nitration of this residue under these experimental conditions. At higher concentrations of peroxynitrite (600–1000 μM), other peptides containing Tyr¹⁷⁷ (solvent-exposed) were also found nitrated (Table 2). In the case of Fe-SODA, the critical Tyr (Tyr³⁶ in the crystal structure; see below) was also preferentially nitrated after exposure to 100 μM peroxynitrite, being detected on a dinitrated peptide containing Tyr³⁶ and Tyr²⁹ (Table 2).

Total 3-nitrotyrosine quantification was performed for both *T. cruzi* Fe-SODs isoforms after peroxynitrite treatment (0–3000 and 0–100 μM peroxynitrite for Fe-SODB and Fe-SODA, respectively) in order to accurately correlate enzyme inactivation with Tyr nitration. Control and peroxynitrite-treated Fe-SODB were analyzed, and the results are shown in Table 3. Results are expressed as the ratio of 3-nitrotyrosine/SOD monomer, and theoretical 3-nitrotyrosine values were calculated assuming enzyme inactivation to be due to the sole nitration of one Tyr per Fe-SOD monomer (*i.e.* Tyr³⁵ in Fe-SODB), and thus 100% inactivation must yield a 3-nitrotyrosine/SOD ratio of 1. For Fe-SODB treated with peroxynitrite at pH 8, a linear correlation between the percentage of enzyme inactivation and total 3-nitrotyrosine quantification was observed, clearly indicating that peroxynitrite-mediated enzyme inactivation is due to the selective nitration of Tyr³⁵ (although the solvent-accessible Tyr¹⁷⁷ was also found nitrated but had a small contribution to total 3-nitrotyrosine). In the case of Fe-SODA, a larger yield of tyrosine nitration and the extent of enzyme inactivation was observed at a smaller peroxynitrite concentration at pH 8 in comparison with Fe-SODB (Table 3). Under this condition, the quantitated experimental value of 3-nitrotyrosine by LC-MS/MS was somewhat less than that predicted from the loss of activity, which may be due to the fact that other Tyr oxidative modifications were observed by MALDI-TOF/MS (Table 2) and may contribute to inactivation, a hypothesis that needs further confirmation. Interestingly, peroxynitrite treatment of Fe-SODA at pH 5.8 revealed experimental 3-nitrotyrosine quantitation higher than the predicted one from the observed 16% of enzyme inactivation (Table 3), in good agreement with the nitration of non-critical solvent-exposed tyrosines via $\cdot\text{NO}_2$ and $\cdot\text{OH}$ formed in the bulk from ONOOH homolysis.

Crystal Structure of *T. cruzi* Mitochondrial Fe-SODA and Differences from Cytosolic Fe-SODB—In order to understand the contrasting behaviors of both Fe-SOD isoforms toward peroxynitrite-mediated inactivation, we solved the crystal structure of the mitochondrial *T. cruzi* Fe-SODA (Table 4) and compared it with the previously reported structure of cytosolic Fe-SODB (Protein Data Bank entry 2GPC) (76). The Fe-SODA structure revealed a tightly bound dimer in the asymmetric unit (Fig. 6A), the two protomers related by a strong non-crystallographic 2-fold axis. The total buried area due to dimerization is high ($\sim 1900 \text{ \AA}^2$), consistent with the dimeric behavior of Fe-SODA in solution. The overall structure of Fe-SODA is similar to those of previously solved iron SODs (76, 77). The nomenclature of secondary structure elements is depicted on one of the Fe-SODA monomers in Fig. 6B. Each monomer binds one iron cation within the metal-binding pocket between the two domains. The metal is pentacoordinated to His²⁸-Ne2 (in helix $\alpha 1$), His⁷⁹-Ne2 ($\alpha 3$), Asp¹⁶³-O $\delta 2$ ($\beta 3$), His¹⁶⁷-Ne2 (in the helical linker loop connecting $\beta 3$ with $\alpha 6$), and a water molecule (HOH7 in chain A and HOH6 in chain B). As in other iron SODs, the metal coordination geometry is trigonal bipyramidal, with His⁷⁹, His¹⁶⁷, and Asp¹⁶³ as equatorial ligands and the His²⁸ and water oxygen axial. *T. cruzi* mitochondrial Fe-SODA is structurally very similar to cytosolic Fe-SODB with a root mean square deviation of 0.75 \AA , superimposing one monomer

TABLE 2

Peroxynitrite-modified tyrosine-containing peptides in *T. cruzi* Fe-SODs detected by MALDI-TOF mass spectrometry

MALDI-TOF/TOF mass spectrometry analysis was carried out in control and peroxynitrite-treated purified recombinant *T. cruzi* Fe-SODs. Fe-SODB and Fe-SODA were treated with increasing peroxynitrite concentrations (0–1000 μM), and enzyme activity was assayed. After treatment, control and treated enzymes were subjected to SDS-gel electrophoresis, and protein bands were in-gel digested with trypsin (sequence grade). Digested proteins were analyzed by MALDI-TOF mass spectrometry, and peptides were searched in the MASCOT database. Ox, oxidation; Mo, monoisotopic. Numbering corresponds to the position observed in the crystal structure of both *T. cruzi* Fe-SODs.

Peroxynitrite	Mo Observed mass (M + H) ⁺	Mo Theoretical mass (M + H) ⁺	Assigned sequence
μM	Da	Da	
Fe-SODB			
150	2127.09	2127.04	²¹ K.QQVTLH ²⁸ YDKHHQG ³⁵ YVTK ³⁸ + Nitro(Y)
600	2127.00	2127.04	²¹ K.QQVTLH ²⁸ YDKHHQG ³⁵ YVTK ³⁸ + Nitro(Y)
	1014.46	1014.47	³⁰ K.HHQG ³⁵ YVTK ³⁸ + Nitro(Y)
	2156.00	2156.03	¹⁷² K.NDRAA ¹⁷⁷ YVQTFWNVNWK ¹⁸⁸ + Nitro(Y)
	1770.82	1770.86	¹⁷⁵ R.AA ¹⁷⁷ YVQTFWNVNWK ¹⁸⁸ + Nitro(Y)
	2269.10	2269.11	¹⁷⁵ R.AA ¹⁷⁷ YVQTFWNVNWK ¹⁸⁸ + Nitro(Y)
1000	2127.08	2127.04	²¹ K.QQVTLH ²⁸ YDKHHQG ³⁵ YVTK ³⁸ + Nitro(Y)
	1770.88	1770.86	¹⁷⁵ R.AA ¹⁷⁷ YVQTFWNVNWK ¹⁸⁸ + Nitro(Y)
	2269.17	2269.11	¹⁷⁵ R.AA ¹⁷⁷ YVQTFWNVNWK ¹⁸⁸ + Nitro(Y)
Fe-SODA			
100	3095.54	3095.50	¹⁴ DGCAVLSRQLELH ²⁹ YTKHHKA ³⁶ YVDK ⁴⁰ + 2Nitro(Y)
	2096.02	2096.06	¹⁵⁵ GLRPVFTVDVWEHA ¹⁶⁹ Y ¹⁷⁰ YK ¹⁷¹ + Ox(Y)
	3337.64	3337.66	¹⁷⁷ RVD ¹⁸⁰ YLKEIWTIVDWEFVSR ¹²⁷ YEQAMK ¹³² + Ox(Y) + Ox(M)
150	2868.39	2868.39	⁴⁰ LNALAGAT ⁴⁸ YDGKT ⁵³ MEDIIVALANDSEK ⁶⁶ + Nitro(Y)
	2884.37	2884.39	⁴⁰ LNALAGAT ⁴⁸ YDGKT ⁵³ MEDIIVALANDSEK ⁶⁶ + Nitro(Y); Ox(M)
	2096.03	2096.06	¹⁵⁵ GLRPVFTVDVWEHA ¹⁶⁹ Y ¹⁷⁰ YK ¹⁷¹ + Ox(Y)
	2125.03	2125.04	¹⁵⁵ GLRPVFTVDVWEHA ¹⁶⁹ Y ¹⁷⁰ YK ¹⁷¹ + Nitro(Y)
	2112.03	2112.06	¹⁵⁵ GLRPVFTVDVWEHA ¹⁶⁹ Y ¹⁷⁰ YK ¹⁷¹ + 2Ox(Y)
	2314.16	2314.17	¹⁷⁸ VD ¹⁸⁰ YLKEIWTIVDWEFVSR ¹⁹⁵ + Ox(Y)

TABLE 3

3-Nitrotyrosine quantification of peroxynitrite-treated *T. cruzi* Fe-SODs by LC-MS/MS

After peroxynitrite treatment (0–1500 μM), *T. cruzi* Fe-SODs were hydrolyzed overnight at 116 °C in HCl (6 N), and pellet was resuspended in formic acid (0.1%, v/v) and analyzed by LC-MS/MS as described under “Experimental Procedures.” Theoretical NO₂-Tyr was calculated assuming that enzyme inactivation is due to the selective nitration of only one Tyr per enzyme monomer (*i.e.* Tyr³⁵ in Fe-SODB or Tyr³⁶ in Fe-SODA). Results are expressed as NO₂-Tyr/SOD monomer.

	ONOOH	Fe-SOD activity	Experimental nitrotyrosine/SOD monomer	Theoretical nitrotyrosine/SOD monomer	
	μM	%			
Fe-SODB (pH 8)	0	100	0	0	
	500	82.8	0.18	0.17	
	1500	74.5	0.29	0.26	
	3000	35	0.66	0.65	
Fe-SODA					
	pH 8	0	100	0.03	0
		100	56	0.26	0.43
	pH 5.8	100	84	0.33	0.16

(843 atoms) and 1.14 Å aligning the whole dimer (1843 atoms). In particular, the identities and positions of the iron-binding residues in the active sites are absolutely conserved, including the axial water molecules. In the folded state of Fe-SOD, as represented by the crystal structure, the metal cation is seen completely buried within its binding pocket, with no connection to the solvent-accessible surface of the protein. An outer, second shell of residues with respect to the ones acting as direct iron ligands can be identified, interacting with the coordinating shell, and/or delimiting bulk solvent channels toward the metal pocket (Fig. 6C). These second shell residues are also positioned in the same way in both Fe-SOD isoforms, and they include critical Tyr³⁵ (78) at 5.6 Å from the metal center. Further extending our structural analysis, there are differences between Fe-SODA and Fe-SODB, which concern Cys and Trp amino acids. Among the four cysteine residues present in Fe-SODA (Cys¹⁶, Cys⁸⁵, Cys¹³¹, and Cys¹⁵⁰) and the three in Fe-SODB (Cys⁸³ (which is observed in its oxidized sulfonic state in the

TABLE 4

Crystal structure of mitochondrial Fe-SODA

Shown are data collection and refinement statistics.

Space group	P2 ₁
Protein molecules per asymmetric unit	2
Solvent content (%)	43.4
Wavelength (Å)	1.5418
Data resolution (Å) ^a	24.17–2.23 (2.35–2.23)
Measured reflections	133337
Multiplicity ^a	7.1 (6.8)
Completeness (%) ^a	98.8 (95.7)
R _{meas} (%) ^{a,b}	9.9 (43.2)
$\langle I/\sigma(I) \rangle^a$	18.5 (5.4)
<i>a</i> , <i>b</i> , <i>c</i> (Å)	47.17, 74.55, 56.85
β (degrees)	96.8
Refinement resolution (Å)	24.17–2.23
R _{cryst} ^c (no. of reflections)	0.168 (17,522)
R _{free} ^c (no. of reflections)	0.219 (1368)
Root mean square, bonds (Å)	0.01
Root mean square, angles (degrees)	1.1
Protein non-hydrogen atoms	3227
Water atoms	102
Iron atoms	2
Mean <i>B</i> factor, overall: chain A/chain B (Å ²)	28/29
Mean <i>B</i> factor, main chain: chain A/chain B (Å ²)	26/27
Mean <i>B</i> factor, side chains: chain A/chain B (Å ²)	30/31
Mean <i>B</i> factor, waters (Å ²)	30
Mean <i>B</i> factor, liganded iron (Å ²)	17.8
Map versus model correlation coefficient (overall/local) ^d	0.889/0.919
No. of residues in Ramachandran plot regions ^e (allowed/favored/outliers)	402/390/0
Protein Data Bank code	4DVH

^a Values in parentheses apply to the high resolution shell.

^b $R_{meas} = \sum_i \sqrt{N_i} / (N_i - 1) \sum_j |I_j - \langle I \rangle| / \sum_j I_j$, where *N_i* represents multiplicity for each reflection; *I_j* is the *j*th observation of reflection *h*; and $\langle I \rangle$ is the mean of the intensity of all observations of reflection *h*, with $I \pm = 1/N_i \sum_j (I(-) \text{ or } I(+))$. \sum_i is taken over all reflections. \sum_j is taken over all observations of each reflection.

^c $R = \sum_h |F(h)_{obs} - F(h)_{calc}| / \sum_h |F(h)_{obs}|$; *R*_{cryst} and *R*_{free} were calculated using the working and test *hkl* reflection sets, respectively.

^d Calculated with Phenix get_cc_mtz_pdb (92).

^e Calculated with Molprobit (42).

structure), Cys¹⁴⁶, and Cys¹⁵⁹), only one is conserved; Cys¹⁵⁰ in Fe-SODA is structurally equivalent to Cys¹⁴⁶ in Fe-SODB (Fig. 7). The four Cys side chains in mitochondrial Fe-SODA are

Peroxynitrite-mediated Inactivation of *T. cruzi* Fe-SODs

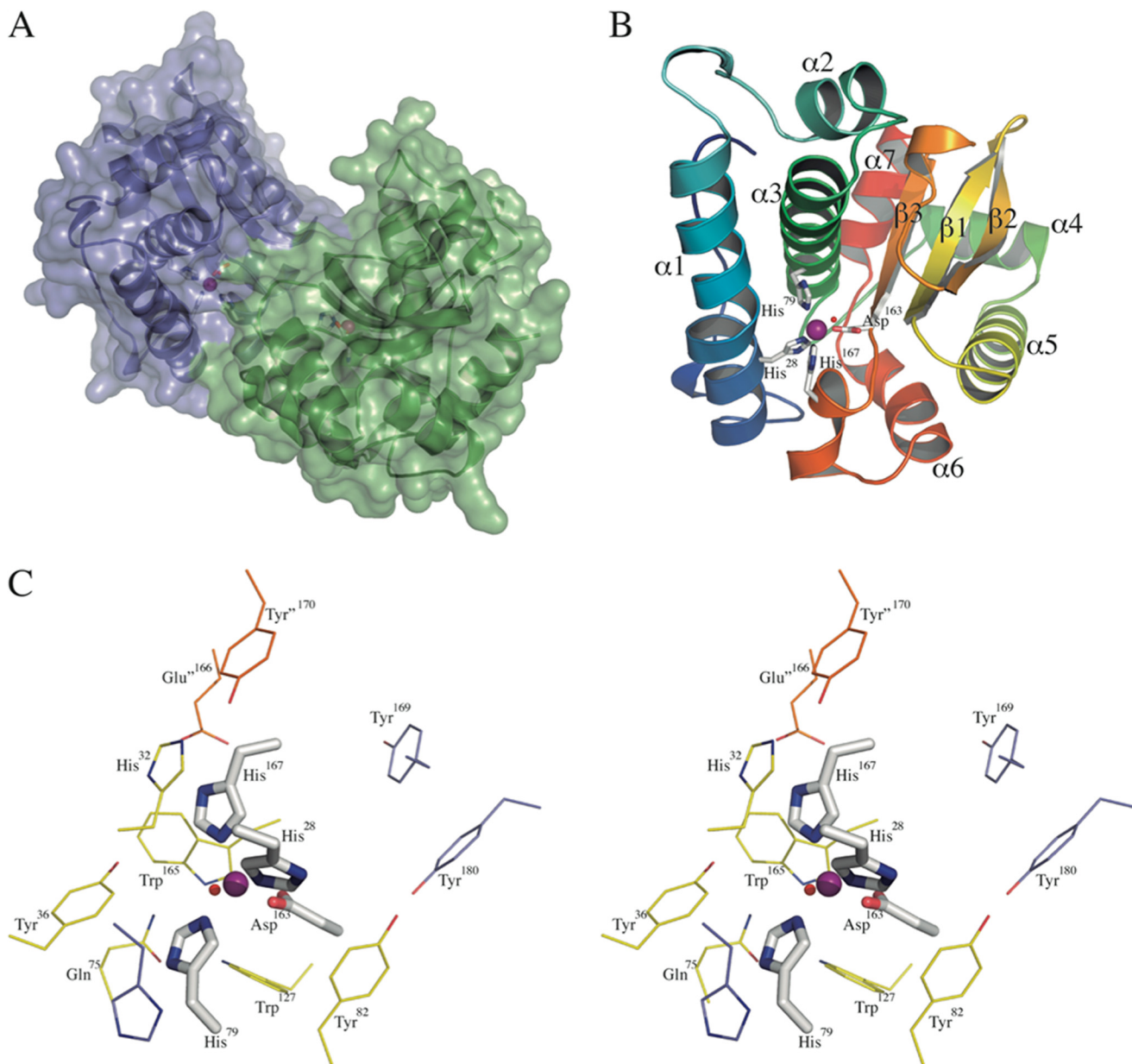


FIGURE 6. Crystal structure of *T. cruzi* mitochondrial Fe-SODA. *A*, solvent-accessible surface representation of the *T. cruzi* Fe-SODA dimer. The surface is rendered semitransparent to observe the secondary structure organization underneath, drawn as a schematic. Each protomer is highlighted with different colors. The active sites are depicted with spheres (iron atoms in purple and coordinating waters in red) and sticks for the coordinating amino acids. *B*, schematic representation of one Fe-SODA monomer (chain B) with a color ramp to indicate the N terminus (blue) to C terminus (red) direction. Helices are labeled from $\alpha 1$ to $\alpha 7$, and β -sheets are labeled from $\beta 1$ to $\beta 3$. Note the conserved bulge in $\alpha 1$. The metal-binding active site is shown as in *A*, with the coordinating residues labeled (water HOH6, red sphere, is unlabeled for clarity). *C*, stereo view of the active site, highlighting the first sphere of direct iron coordination residues in labeled sticks (colored by atom, with carbon in gray, nitrogen in blue, and oxygen in red). The coordinating water (red sphere) is not labeled for clarity. A second sphere of residues, in contact with the first sphere and/or defining entrance channels to the iron-binding pocket, are shown as lines colored by atom (with carbon in yellow, for the same monomer, or orange for the other monomer in the dimer). The critical Tyr³⁶ is observed on the left. A more distant shell is also shown as lines (His³³, Tyr¹⁶⁹, and Tyr¹⁸⁰), with carbon atoms in blue.

solvent-accessible in the crystal structure, in agreement with the data obtained by sulfhydryl titration (four DTNB-reactive thiols per monomer). In contrast, Fe-SODB displays only two of its Cys thiols accessible to bulk solvent (Cys⁸³ and Cys¹⁴⁶). Fe-SODB Cys¹⁵⁹ is instead buried within the folded protein core, at 9.9 Å from the iron atom, again consistent with the thiol titration (2 DTNB-reactive thiols/monomer). Analysis of the Trp residues reveals that, apart from a conserved core of five tryptophans in both isoforms, key differences are uncovered in a critical region: the funnel entrance toward the metal-binding

pocket, in the interface between helices $\alpha 1$ and $\alpha 3$, including also the rather long initial N-terminal loop that precedes $\alpha 1$. In the cytosolic Fe-SODB structure, Trp⁹ and Trp⁷⁹ (Fig. 7B) are observed located at 11.6 and 6.6 Å, respectively, from the active site iron. These two residues are substituted by phenylalanines in the mitochondrial Fe-SODA. Instead, Fe-SODA locates Trp¹² (substituted by Tyr¹¹ in Fe-SODB) within the N-terminal loop but pointing its side chain away with respect to the entrance channel. Overall, the structural differences in Cys and Trp residues comparing the two *T. cruzi* Fe-SOD isoforms

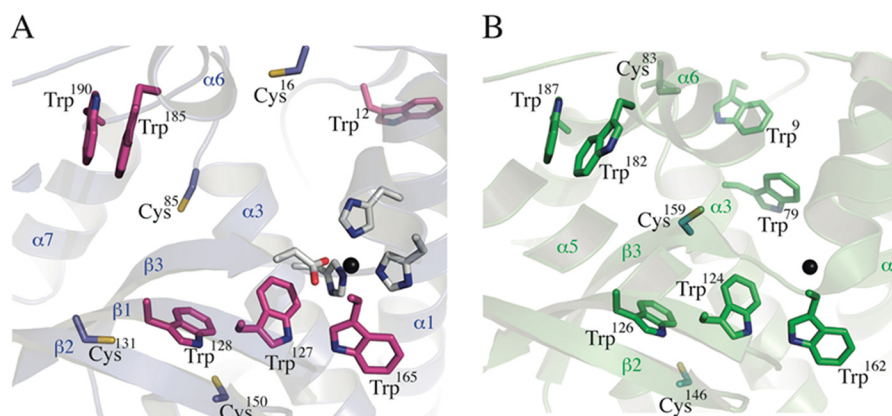
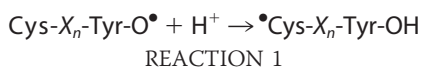


FIGURE 7. **Comparative positions of cysteines and tryptophans in Fe-SODA and Fe-SODB.** A, *T. cruzi* Fe-SODA structure. All of the Cys and Trp residues are labeled and highlighted in stick representation, colored by atom (nitrogen in blue, sulfur in yellow, oxygen in red, and carbon differentially slate blue for Cys and magenta for Trp). As a reference, the active site is shown with the iron atom in dark gray and the first shell of coordinating residues in sticks (colored by atom with carbon in white). The coordinating water is not shown. An underlying schematic is drawn semitransparent, with labels for some of the secondary structure elements. B, *T. cruzi* Fe-SODB structure (Protein Data Bank entry 2GPC). In the same orientation as Fe-SODA (A), Cys and Trp are labeled and highlighted in stick representation, colored by atom (nitrogen in blue, sulfur in yellow, carbon in green). Only the iron atom is shown as a reference in spheres (dark gray), and underlying semitransparent schematic to localize secondary structure elements.

could explain their different susceptibilities to peroxynitrite-mediated inactivation and nitration. The structural data are thus consistent with the existence of an IET mechanism in Fe-SODB involving Cys, Trp and the active site tyrosine residue, as observed previously for other proteins (33, 79, 80).

Insights for the Resistance of Cytosolic Fe-SODB to Peroxynitrite-mediated Inactivation—Cysteine residues can repair tyrosyl radicals in proteins via IET (44). The overall reaction with a peptide sequence can be exemplified as follows.



By this mechanism, the radical character initially located in a tyrosine residue is transferred to a cysteine residue, and therefore further tyrosine oxidative modifications, including tyrosine nitration (by the combination reaction of tyrosyl radical with NO_2), are inhibited. In the case of Fe-SODB, the possible contribution of Cys residues to the resistance to peroxynitrite was explored at different levels. There are two solvent-accessible thiols (Cys⁸³ and Cys¹⁴⁶) in Fe-SODB from a total of three (as measured with DTNB and by crystal structure analysis; Fig. 7). Blockage of the accessible thiols in Fe-SODB with NEM rendered the enzyme significantly more susceptible to peroxynitrite-mediated inactivation (Fig. 8A), whereas no alterations in sensitivity were observed for NEM-treated Fe-SODA (all four Cys residues in Fe-SODA are solvent-accessible as measured with DTNB and by crystal structure analysis; Fig. 7). These results support the participation of the Fe-SODB solvent-accessible Cys (Cys⁸³ and/or Cys¹⁴⁶) in the resistance toward peroxynitrite. Previous mechanistic studies using Tyr-Cys-containing peptides (44, 80, 81) showed that IET (shown in Reaction 1) is mediated by a proton-coupled electron transfer mechanism that involves as a first key step the deprotonation of the Cys residue, which then in the thiolate form acts as the electron donor, followed by IET, yielding the final radical Cys-S[•] (44). To analyze the probability that any of the Cys residues present in *T. cruzi* Fe-SODs could participate in Tyr-O[•] repair

involving an IET process, we first estimated each Cys pK_a value using the propKa software (54–57). The results obtained show that the predicted pK_a values of the Cys present in mitochondrial Fe-SODA (Cys¹⁶, Cys⁸⁵, Cys¹³¹, and Cys¹⁵⁰) and Fe-SODB (Cys¹⁴⁶ and Cys¹⁵⁹) are similar to that observed for free Cys (~8.2–8.3), making less likely the existence of deprotonated forms at pH 7.4. Interestingly, the pK_a value predicted for Fe-SODB Cys⁸³ is approximately 2 pH units lower than the one obtained for the other Cys residues. This lower pK_a can be explained by the presence in its immediate environment of two positively charged residues, Lys¹⁸⁸ and Arg¹⁹². The Lys¹⁸⁸-N ϵ is located at 5.5 Å from the Cys⁸³-S γ and Arg¹⁹²-C ξ at 8.2 Å, increasing the chance for the thiol group to be partially charged at pH 7.4. The Fe-SODB critical Tyr³⁵ is located >20 Å away from Cys⁸³; thus, to repair Tyr³⁵-O[•], a long range IET needs to occur. In this case, relay amino acids (e.g. Trp⁹ and Trp⁷⁹) in the electron transfer pathway are required to improve the efficiency of the process (82, 83). To analyze possible IET pathways in cytosolic Fe-SODB, we performed 20-ns-long MD simulations of the corresponding homodimer, with Tyr³⁵ described as radical, and Cys⁸³ as thiolate (as predicted for its lower pK_a) (i.e. tyrosyl radical-thiolate Fe-SODB system). We then computed possible IET paths between both residues using the pathways algorithm as described under “Experimental Procedures” (44). The resulting most probable IET path comprises the participation of key residues that contributes to the process: Trp⁷⁹ and His³² (Fig. 8B). The presence of aromatic residues along the IET pathway (Trp⁷⁹ and Trp⁹, absent in the Fe-SODA crystal structure) could increase the overall IET rate, as was recently shown (49, 52). In summary, the *in silico* analysis of the tyrosyl radical-thiolate Fe-SODB system strongly suggests that the partially charged Cys⁸³-S⁻ acts as the electron source to rescue critical Tyr³⁵-O[•] formed after peroxynitrite treatment, preventing nitration and inactivation of cytosolic Fe-SODB.

Detection of Cys⁸³-S[•] after the Reaction of Fe-SODB with Peroxynitrite—If an IET mechanism is operative after peroxynitrite reaction with Fe-SODB, a protein radical corre-

Peroxynitrite-mediated Inactivation of *T. cruzi* Fe-SODs

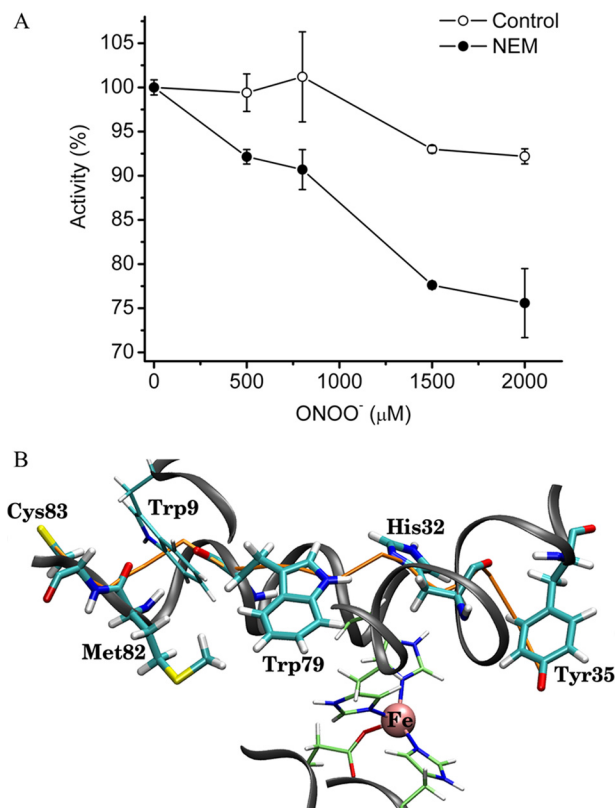


FIGURE 8. Participation of solvent-accessible Fe-SODB thiols in the resistance to peroxynitrite and role of intramolecular electron transfer. *A*, effects of sulfhydryl-blocked Fe-SODB in the reaction with peroxynitrite. Peroxynitrite (0–2000 μM) was added to control (empty circles) or NEM-blocked sulfhydryl Fe-SODB (filled circles) (8 μM) in sodium phosphate buffer (100 mM) at pH 7.4. Activity is expressed as percentage activity relative to the native enzyme or NEM-treated enzyme in the absence of peroxynitrite (100% activity). *B*, selected snapshot for Fe-SODB intramolecular electron transfer pathway from Cys⁸³-S⁻ to Tyr³⁵-O⁻. The figure shows the path for IET as predicted with the pathways algorithm and taken from the explicit water MD simulation (see “Experimental Procedures” for details). Fe-SODB is shown as a black ribbon representation, and the residues Cys⁸³, Met⁸², Trp⁹, Trp⁷⁹, His³², and Tyr³⁵ are shown as boldface sticks. The iron atom is shown as a pink sphere with the coordination residues as cylindrical representations. The predicted IET path is shown in orange and involves electron transfer starting on the Cys⁸³-S atom sequentially to Met⁸², Trp⁷⁹, and His³² and ending in the aromatic ring of Tyr³⁵-O⁻. Parts of the pathway occur through the backbone, and others occur through space. Surrounding waters were omitted for clarity. Error bars, S.E.

sponding to Fe-SODB-Cys⁸³-S⁻ generated in this process should be experimentally detected (Reaction 1). Immunospin trapping and EPR spin trapping analysis were performed in order to detect the protein thiyl radical. Control or NEM-treated Fe-SODB (5 μM) was exposed to peroxynitrite (0–20 μM) in the presence of the spin trap DMPO (100 mM). Importantly, low concentrations of peroxynitrite were used to favor its preferential reaction with the metal center in Fe-SOD and to minimize homolysis because the latter can render thiyl radical by reactions of [•]OH and [•]NO₂ with cysteine independent of the IET mechanism. DMPO-nitronone adducts were detected by Western blot using the anti-DMPO-nitronone antibody as described previously (33, 80). Results show that the covalently DMPO-nitronone adducts detected in Fe-SODB control conditions were significantly inhibited in NEM-treated Fe-SODB, strongly suggesting the generation of Cys⁸³-S⁻ after peroxynitrite reaction with the enzyme (Fig. 9). Moreover, the shift to acidic pI values of native Fe-SODB (major spot pI = 7.5) after

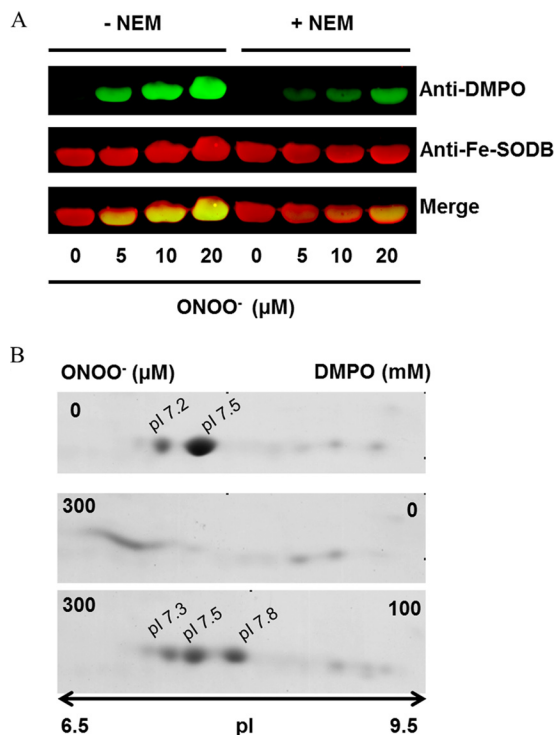


FIGURE 9. Immunospin trapping of protein thiyl radical in the peroxynitrite reaction with Fe-SODB. *A*, control or thiol-blocked NEM-treated Fe-SODB (50 μM) was exposed to peroxynitrite (0–20 μM) in sodium phosphate buffer (100 mM, pH 7.4) in the presence of the spin trap DMPO (100 mM). Immunoreactive proteins were detected with anti-DMPO nitronone antibody (green) and specific anti-Fe-SODB antibody (red). Merged bands are shown in yellow. *B*, two-dimensional gel electrophoresis of *T. cruzi* Fe-SODB (8 μM) treated with peroxynitrite (300 μM) in sodium phosphate buffer (0.2 M) at pH 7.4 and 25 °C in the presence and absence of DMPO (100 mM). Two-dimensional gel electrophoresis was performed as described under “Experimental Procedures.”

peroxynitrite treatment (<7.2) was prevented in the presence of DMPO with a new more basic spot (pI = 7.8) probably corresponding to the Fe-SODB-DMPO adduct (Fig. 9B).

Furthermore, EPR spin trapping analysis of the reaction of Fe-SODB (2 mM) with peroxynitrite (500 μM) was performed in the presence of the spin trap PBN (50 mM). Again, reaction conditions were optimized to favor the direct reaction of peroxynitrite with Fe-SODB and to obtain detectable EPR signals. The addition of peroxynitrite to Fe-SODB led to the detection of an EPR spectrum characteristic of a strongly immobilized nitroxide adduct (Fig. 10A). The spin adduct was subjected to nonspecific proteolysis with Pronase, resulting in the conversion of the spectrum into an isotropic six-line spectrum characteristic of PBN-protein thiyl adducts (Fig. 10B) (84–86). In order to confirm that the EPR signal observed was due to the formation of Cys⁸³-S⁻ after peroxynitrite reaction, the Fe-SODB mutant C83S was generated. In this case, the PBN-protein radical adduct was almost completely inhibited (Fig. 10, C and D), demonstrating the generation of Cys⁸³-S⁻.

The Role of Cys⁸³ in the Inhibition of Tyr³⁵ Nitration via IET; Studies with Mutant Fe-SODB and Free Thiols—In order to confirm the participation of Cys⁸³ in the IET mechanism proposed, site-directed mutagenesis experiments were performed. First, our primary candidate for the IET process was the Cys¹⁵⁹ located at 9.9 Å from the iron atom of the active site of Fe-

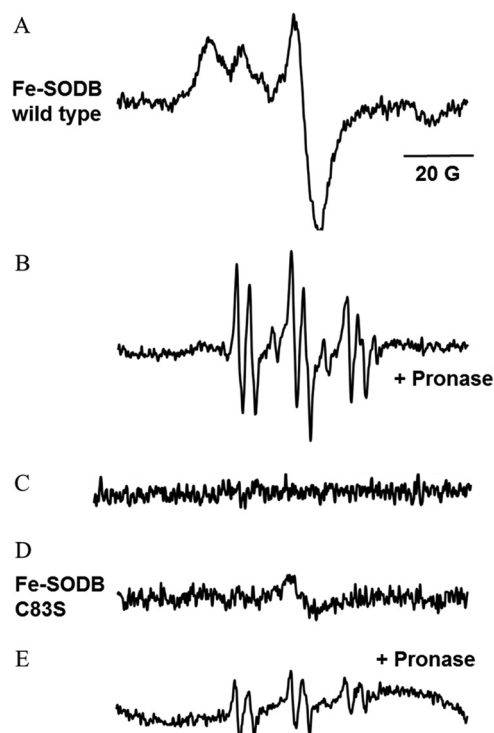


FIGURE 10. EPR spectra of PBN-protein radical adducts obtained in the peroxynitrite reaction with Fe-SODB. The spectra were obtained after a 1-min incubation at room temperature of wild type Fe-SODB or C83S mutant (2 mM) in the presence of PBN (50 mM) and peroxynitrite (500 μ M) in phosphate buffer (0.1 M). *A*, wild type Fe-SODB; *B*, wild type Fe-SODB treated with Pronase (20 mg/ml for 10 min). *C*, wild type Fe-SODB without peroxynitrite. *D*, C83S Fe-SODB; *E*, C83S treated with Pronase (20 mg/ml for 10 min). Instrumental conditions were as follows: microwave power, 20 milliwatts; modulation amplitude, 1.0 G; time constant, 164 ms; gain, 5×10^5 .

SODB and not present in the crystal structure of Fe-SODA. Mutation of Cys¹⁵⁹ (C159S) did not affect the resistance of Fe-SODB to peroxynitrite-dependent inactivation, indicating that this residue was not participating in the IET process (Fig. 11*B*). Importantly, mutation of the single Cys⁸³ (C83S) rendered the enzyme more susceptible to peroxynitrite-mediated inactivation as compared with wild type Fe-SODB (Fig. 11*C*). Moreover, we also generated the double mutant N187D/K189E, which completely modifies the protein environment adjacent to Cys⁸³ from a net positively charged to a negatively charged one. This change of microenvironment is expected to result in a significant increase in Cys⁸³ p*K*_a, with a consequent decrease of the amount of Cys-S⁻ necessary to repair the critical Tyr³⁵-O[•]. Indeed, N187D/K189E Fe-SODB significantly lost the resistance against peroxynitrite treatment when compared with the wild type protein, reinforcing the role of Cys⁸³ in the IET proposed mechanism (Fig. 11*D*).

It has been shown that thiols are the dominant “sink” for peroxynitrite and [•]NO₂ in cells (28, 87). The calculated rate constant of [•]NO₂ with GSH and Cys is 2 and 5×10^7 M⁻¹ s⁻¹, respectively (28). This scavenging reaction may prevent the [•]NO₂-dependent tyrosine nitration and thus enzyme inactivation (28, 72). In order to examine whether Cys⁸³ could contribute to the inhibition of enzyme inactivation via direct [•]NO₂ scavenging, we performed experiments using the Fe-SODB C83S mutant in the presence of equimolecular amounts of the

more reactive L-cysteine methyl ester (8 μ M; p*K*_a ~6.7 (88)). The presence of this [•]NO₂ radical scavenger failed to protect Fe-SODB-C83S mutant from peroxynitrite inactivation, strongly suggesting that the protection observed in wild type Fe-SODB by Cys⁸³ was mainly mediated by an IET and not by [•]NO₂ free radical scavenging (Fig. 11*C*). It is important to note that although mutation of Cys⁸³ in Fe-SODB renders the enzyme more susceptible to oxidant-dependent inactivation, it was still more resistant than Fe-SODA. This result indicates that other residues, probably Trp⁷⁹ and Trp⁹, may be additionally participating in Tyr³⁵-O[•] repair after peroxynitrite treatment.

Fe-SODA Modifications during Cellular Nitroxidative Stress Conditions to T. cruzi—Fe-SODA *T. cruzi* overexpressers (12, 58) were used to search for modifications of Fe-SOD occurring during nitroxidative stress conditions in living parasites (epimastigote stage). Following the induction of Fe-SODA expression by tetracycline (4–6-fold increase respect to wild type), parasites were incubated in the presence of antimycin A (complex III electron chain inhibitor) plus a [•]NO donor, in order to specifically generate peroxynitrite at the mitochondrial cell compartment (59). Following treatment, parasites protein extracts were separated by two-dimensional electrophoresis and probed with anti-Fe-SODs antibodies. After AA/[•]NO treatment, an important shift toward more acidic pH values in the pI of Fe-SODA was evident (Fig. 12). This pI shift was also observed during exogenous peroxynitrite challenge to parasites (Fig. 12*A*). The pI changes observed in Fe-SODA obtained from living parasites during exposure to either endogenous (AA/[•]NO) or exogenous peroxynitrite were similar to those observed for the recombinant Fe-SODA after peroxynitrite treatment (Fig. 5*A*). Notably, Fe-SODB was not significantly altered under these cellular nitroxidative conditions, in agreement with its high resistance to peroxynitrite.

The pI changes in Fe-SODA during nitroxidative challenge to living parasites correlated reasonably well with the extents of protein tyrosine nitration (Fig. 12*B*). Indeed, endogenous and exogenous fluxes of peroxynitrite (AA/[•]NO or the peroxynitrite donor SIN-1, respectively) caused nitration of parasite proteins. Immunoprecipitation analysis of Fe-SODA revealed the presence of nitrated enzyme in the SIN-1-treated parasites, unambiguously revealing the reaction of nitrating species and subsequent oxidative postranslational modifications of Fe-SODA in living parasites (Fig. 12*C*). Overall, the data in Fig. 12 confirm the feasibility of these biochemical events in Fe-SODA as biologically relevant processes.

DISCUSSION

T. cruzi mitochondrial and cytosolic Fe-SODs were purified to homogeneity as active enzymes with specific activities and O₂^{-•} dismutation rates comparable with those of other Mn- and Fe-SODs. Similarly, both SODs readily reacted with peroxynitrite at comparable second order rate constants ($\sim 4.5 \times 10^4$ M⁻¹ s⁻¹) (Table 1) (18, 33, 62, 63) and were dose-dependently inactivated and nitrated by peroxynitrite (Fig. 3).

Peptide mapping by mass spectrometry analysis of the peroxynitrite-treated enzymes together with 3-nitrotyrosine quantification revealed that peroxynitrite-dependent inactiva-

Peroxynitrite-mediated Inactivation of *T. cruzi* Fe-SODs

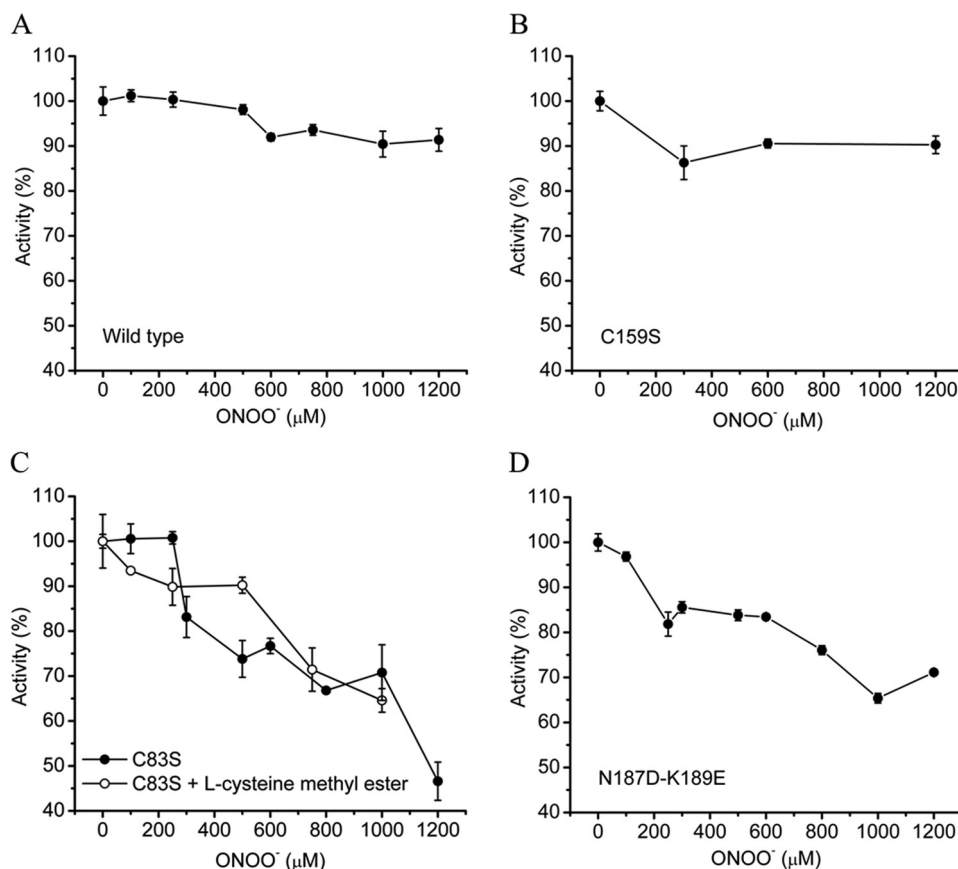


FIGURE 11. Peroxynitrite reaction with Fe-SODB mutants; role of Cys⁸³. Fe-SODB wild type (A) or mutants (C159S (B), C83S (C), and N187D/K189E (D)) (8 μM) were exposed to peroxynitrite (0–1200 μM) in sodium phosphate buffer (100 mM, pH 7.4), and residual SOD activity was measured as previously. In C, C83S Fe-SODB was also exposed to peroxynitrite in the presence (empty circles) of L-cysteine-methyl ester (8 μM, p*K*_a = 6.5). Error bars, S.E.

tion of *T. cruzi* Fe-SODs is due to the selective nitration of the universally conserved Tyr³⁵ located near the iron atom of the active site, as was previously observed for Mn-SOD and *E. coli* SODs (Fig. 5 and Table 2) (17, 18). The proximal reactive species was the anionic form of peroxynitrite (ONOO⁻), and the primary target at the enzyme was the active site iron atom, as was revealed by pH studies, cysteine alkylation, and CO₂ competition experiments (Figs. 4 and 8 and Table 1).

In the most likely reaction mechanism, the metal-based Lewis adduct formed in the reaction (*i.e.* SOD-Fe^{III}-OONO (89)) undergoes homolysis to yield ·NO₂ and the corresponding oxo-metal complex (SOD-Fe^{IV}=O) (89). This SOD-Fe^{IV}=O complex is strongly oxidizing and promotes the oxidation of Tyr³⁵ to Tyr³⁵-O· that rapidly combines with ·NO₂ generated *in situ* to yield a tyrosine-nitrated enzyme, as proposed in Scheme I. Thus, site specificity is provided by a combination of kinetic factors (fast reaction of peroxynitrite with the iron center in contrast to the much slower proton-catalyzed homolysis) and close structural relationships between the iron atom and the active site tyrosine. Once Tyr³⁵ is nitrated, O₂⁻ dismutation is impeded by both a steric effect (as the nitro group located in the access channel impedes O₂⁻ diffusion) and the electrical charge repulsion provided by the ionization of the phenolic group in Tyr, by analogy with the recently reported data for mammalian Mn-SOD (20, 90).

Although both isoforms were inactivated by peroxynitrite, Fe-SODB was extremely resistant to nitration and inactivation

as compared with its mitochondrial counterpart (Fig. 3). For example, only 20% of Fe-SODB became inactivated at pH 7.4 with high peroxynitrite concentrations (1500 μM), whereas most of the Fe-SODA activity was already lost at 200 μM peroxynitrite, a similar susceptibility to what was reported for *E. coli* Mn- and Fe-SODs and mammalian Mn-SOD (18, 91).

Due to the apparent sequence and structural homology among Fe-SODs of different species, this disparate susceptibility on peroxynitrite-mediated inactivation of *T. cruzi* Fe-SODs was intriguing. Thus, in order to search for structural differences that may explain the high intrinsic resistance to oxidant inactivation of the Fe-SODB isoform, we solved the crystal structure of *T. cruzi* mitochondrial Fe-SODA at 2.2 Å resolution. Comparison of the crystal structures of both isoforms revealed a number of potentially relevant differences to explain the results obtained in our study. Two tryptophans (Trp⁹ and Trp⁷⁹) and two cysteines (Cys⁸³ and Cys¹⁵⁹) are located near the active site of Fe-SODB and are absent in the crystal structure of the mitochondrial counterpart (Fig. 7). It was previously shown that the presence of a cysteine residue in the proximity of a tyrosine might enable radical transfer during one-electron oxidation processes, with the cysteine acting as electron donor (44). In this regard, following peroxynitrite reaction with the iron center of Fe-SODB, the Tyr³⁵-O· generated could be quickly reduced by a cysteine residue back to Tyr³⁵ prior to the nitration step, therefore preventing enzyme inactivation. Of the three cysteines present in Fe-SODB, only Cys⁸³, located

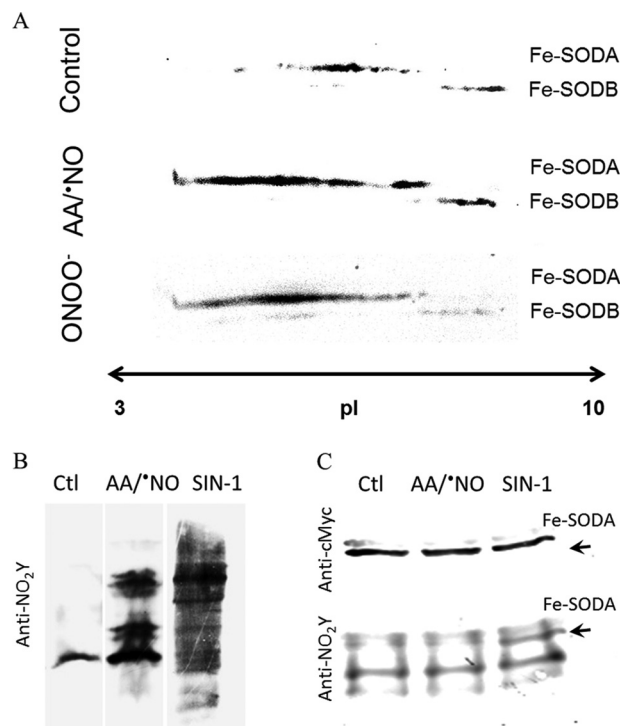
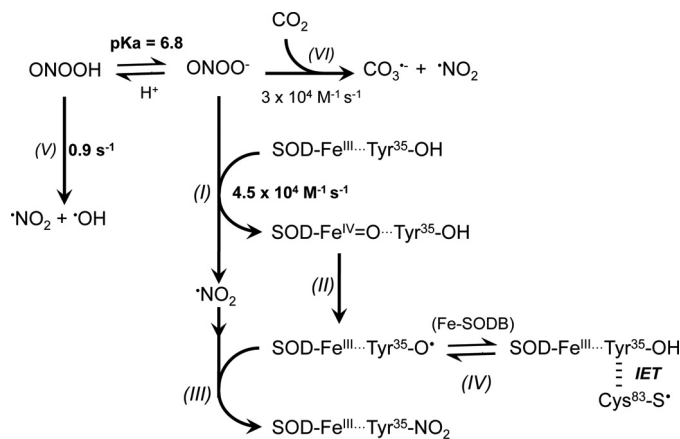


FIGURE 12. Cellular detection of Fe-SODA nitroxidative modifications. *A*, two-dimensional gel electrophoresis. *T. cruzi* Fe-SODA overexpressers were treated with AA (5 μ M) plus NOC-12 (5 mM; $t_{1/2}$ = 100 min at pH 7.4), SIN-1 (5 mM), or ONOO⁻ (300 μ M) for 3 h at room temperature. After treatment, samples were processed as described under "Experimental Procedures" and subjected to two-dimensional electrophoresis. Membranes were probed with the specific Fe-SODA and Fe-SODB antibodies. *B*, 3-nitrotyrosine detection in parasites. Following treatment in the conditions described in *A*, parasite extracts were separated in 15% SDS gels and transferred to nitrocellulose membranes. Membranes were probed with the specific anti-3-nitrotyrosine antibody. *C*, immunoprecipitation of nitrated Fe-SODA. Parasite extracts as above were incubated overnight at 4 °C in the presence of the monoclonal c-Myc antibody that recognized the 9E10 epitope of Fe-SODA in the presence of protein A/G-agarose as described under "Experimental Procedures." Immunoprecipitated proteins were run in 15% SDS-gel electrophoresis, electrotransferred to nitrocellulose, and revealed using anti-c-Myc antibody and anti-3-nitrotyrosine antibody and as described under "Experimental Procedures."

22 Å away from Tyr³⁵, is predicted to have a lower pK_a value favoring the electron transfer process to Tyr³⁵-O[•] (44). Moreover, MD simulations of the tyrosyl radical-thiolate system (Tyr³⁵-O[•]...Cys⁸³-S⁻) in Fe-SODB revealed Trp⁷⁹ and His³² as key residues acting as "relay" amino acids or "stepping stones" for the electron transfer (Fig. 8B). Ultimately, this type of IET process generates a thiyl radical, as observed previously for the hydrogen peroxide-mediated oxidation of myoglobin (80, 81) and peroxynitrite-mediated oxyhemoglobin oxidation (33, 80).

In this work, using different experimental approaches, the Cys⁸³-S⁻ generated in the Fe-SODB after the reaction with peroxynitrite was identified (Figs. 9 and 10), demonstrating the participation of an IET pathway in the observed resistance to peroxynitrite. A further proof of the key role of Cys⁸³ in modulating the redox chemistry at the active site is that the Fe-SODB C83S mutant significantly increased the sensitivity to peroxynitrite-mediated inactivation (Fig. 11C). Future experiments, including additional enzyme mutants, are needed in order to determine the precise amino acids involved in the IET pathway(s) and whether other amino acids can also participate



SCHEME 1. Proposed reaction mechanisms for the reaction of *T. cruzi* Fe-SODs with peroxynitrite. Peroxynitrite anion (ONOO⁻, 80% at pH 7.4) reacts with the Fe^{III} atom of the Fe-SODs, yielding the corresponding oxo-metal complex (SOD-Fe^{IV}=O) with •NO₂ generation (reaction I). SOD-Fe^{IV}=O oxidizes the active site Tyr (Tyr³⁵ in Fe-SODB and Tyr³⁶ in Fe-SODA) to its corresponding tyrosyl radical (SOD-Fe^{III}...Tyr³⁵-O[•]) (reaction II). SOD-Fe^{III}...Tyr³⁵-O[•] rapidly combines with •NO₂ (II), yielding the nitrated and inactivated enzyme SOD-Fe^{III}...Tyr³⁵-NO₂ (reaction III). In *T. cruzi* Fe-SODB (reaction IV), Cys⁸³-S⁻ repairs Fe^{III}...Tyr³⁵-O[•], regenerating Fe^{III}...Tyr³⁵-OH through an IET process. The homolytic cleavage of ONOOH (reaction V) and the nucleophilic addition of ONOO⁻ to CO₂ (reaction VI) (reviewed in Ref. 89) compete with reaction I and decrease the extents of Tyr³⁵ nitration and enzyme inactivation.

in tyrosyl radical repair. From a biological perspective, it is conceivable that the solvent-accessible Cys⁸³-S⁻ can be repaired in living cells by low molecular weight reductants. For instance, molecules, such as glutathione, trypanothione, or ascorbate, present in the *T. cruzi* cytosol may provide a sustained protection to Fe-SODB at the expense of these "sacrificial" antioxidant molecules. In this regard, we were able to detect nitrated Fe-SODA in living parasites exposed to exogenous (SIN-1) or endogenous (AA/*NO) fluxes of peroxynitrite. Whereas in the case of SIN-1, peroxynitrite will be formed and react in various cellular compartments, including cytosol and mitochondria, the AA/*NO treatment leads to the mitochondrial formation of peroxynitrite. In both cases, only substantial post-translational oxidative modifications were observed in Fe-SODA, underscoring the capacity of Fe-SODB to resist peroxynitrite-mediated inactivation. Both an important shift in the pI of Fe-SODA and the detection of nitrated protein (after immunoprecipitation) are indicative of oxidative modifications due to peroxynitrite reactions in mitochondria (Fig. 12). Future experiments using Fe-SODA and Fe-SODB *T. cruzi* overexpressers in infections to macrophages and cardiomyocytes will allow us to evaluate in more detail the biological significance of our results. In particular, the peroxynitrite-mediated inactivation of Fe-SODA may be secondarily responsible for parasite programmed cell death during the infection process. Indeed, the inactivation of Fe-SODA would raise the intramitochondrial O₂⁻ state concentration, which is an apoptotic signal in *T. cruzi* (12). On the other hand, the robust Fe-SODB would resist the oxidative challenge promoted by mammalian host cells and contribute to the neutralization of the oxidative challenge. Thus, as was observed previously for other *T. cruzi* antioxidant enzymes (7), *T. cruzi* Fe-SODs may function as virulence factors, a hypothesis that is currently under investigation in our laboratories both in the cellular and animal models of Chagas

disease. From a chemistry-oriented point of view the data we are now reporting underscore that the extent of peroxynitrite-mediated oxidative modifications in genetically engineered proteins can be modulated taking advantage of long range intramolecular electron transfer processes.

REFERENCES

1. Fridovich, I. (1995) Superoxide radical and superoxide dismutases. *Annu. Rev. Biochem.* **64**, 97–112
2. Stallings, W. C., Patridge, K. A., Strong, R. K., and Ludwig, M. L. (1984) Manganese and iron superoxide dismutases are structural homologs. *J. Biol. Chem.* **259**, 10695–10699
3. Ismail, S. O., Paramchuk, W., Skeiky, Y. A., Reed, S. G., Bhatia, A., and Gedamu, L. (1997) Molecular cloning and characterization of two iron superoxide dismutase cDNAs from *Trypanosoma cruzi*. *Mol. Biochem. Parasitol.* **86**, 187–197
4. Temperton, N. J., Wilkinson, S. R., and Kelly, J. M. (1996) Cloning of an Fe-superoxide dismutase gene homologue from *Trypanosoma cruzi*. *Mol. Biochem. Parasitol.* **76**, 339–343
5. Urbina, J. A. (2010) Specific chemotherapy of Chagas disease: relevance, current limitations and new approaches. *Acta Trop.* **115**, 55–68
6. Lepesheva, G. I., Villalta, F., and Waterman, M. R. (2011) Targeting *Trypanosoma cruzi* sterol 14 α -demethylase (CYP51). *Adv. Parasitol.* **75**, 65–87
7. Piacenza, L., Zago, M. P., Peluffo, G., Alvarez, M. N., Basombrio, M. A., and Radi, R. (2009) Enzymes of the antioxidant network as novel determiners of *Trypanosoma cruzi* virulence. *Int. J. Parasitol.* **39**, 1455–1464
8. Kierszenbaum, F., Knecht, E., Budzko, D. B., and Pizzimenti, M. C. (1974) Phagocytosis: a defense mechanism against infection with *Trypanosoma cruzi*. *J. Immunol.* **112**, 1839–1844
9. Muñoz-Fernández, M. A., Fernández, M. A., and Fresno, M. (1992) Synergism between tumor necrosis factor- α and interferon- γ on macrophage activation for the killing of intracellular *Trypanosoma cruzi* through a nitric oxide-dependent mechanism. *Eur. J. Immunol.* **22**, 301–307
10. Alvarez, M. N., Peluffo, G., Piacenza, L., and Radi, R. (2011) Intraphagosomal peroxynitrite as a macrophage-derived cytotoxin against internalized *Trypanosoma cruzi*: consequences for oxidative killing and role of microbial peroxiredoxins in infectivity. *J. Biol. Chem.* **286**, 6627–6640
11. Valez, V., Cassina, A., Batinic-Haberle, I., Kalyanaraman, B., Ferrer-Sueta, G., and Radi, R. (2013) Peroxynitrite formation in nitric oxide-exposed submitochondrial particles: detection, oxidative damage and catalytic removal by Mn-porphyrins. *Arch. Biochem. Biophys.* **529**, 45–54
12. Piacenza, L., Irigoín, F., Alvarez, M. N., Peluffo, G., Taylor, M. C., Kelly, J. M., Wilkinson, S. R., and Radi, R. (2007) Mitochondrial superoxide radicals mediate programmed cell death in *Trypanosoma cruzi*: cytoprotective action of mitochondrial iron superoxide dismutase overexpression. *Biochem. J.* **403**, 323–334
13. Demicheli, V., Quijano, C., Alvarez, B., and Radi, R. (2007) Inactivation and nitration of human superoxide dismutase (SOD) by fluxes of nitric oxide and superoxide. *Free Radic. Biol. Med.* **42**, 1359–1368
14. MacMillan-Crow, L. A., Crow, J. P., Kerby, J. D., Beckman, J. S., and Thompson, J. A. (1996) Nitration and inactivation of manganese superoxide dismutase in chronic rejection of human renal allografts. *Proc. Natl. Acad. Sci. U.S.A.* **93**, 11853–11858
15. Radi, R., Rodriguez, M., Castro, L., and Telleri, R. (1994) Inhibition of mitochondrial electron transport by peroxynitrite. *Arch. Biochem. Biophys.* **308**, 89–95
16. Ghafourifar, P., Schenk, U., Klein, S. D., and Richter, C. (1999) Mitochondrial nitric-oxide synthase stimulation causes cytochrome *c* release from isolated mitochondria. Evidence for intramitochondrial peroxynitrite formation. *J. Biol. Chem.* **274**, 31185–31188
17. Yamakura, F., Taka, H., Fujimura, T., and Murayama, K. (1998) Inactivation of human manganese-superoxide dismutase by peroxynitrite is caused by exclusive nitration of tyrosine 34 to 3-nitrotyrosine. *J. Biol. Chem.* **273**, 14085–14089
18. Quijano, C., Hernandez-Saavedra, D., Castro, L., McCord, J. M., Freeman, B. A., and Radi, R. (2001) Reaction of peroxynitrite with Mn-superoxide dismutase. Role of the metal center in decomposition kinetics and nitration. *J. Biol. Chem.* **276**, 11631–11638
19. Surmeli, N. B., Litterman, N. K., Miller, A. F., and Groves, J. T. (2010) Peroxynitrite mediates active site tyrosine nitration in manganese superoxide dismutase: evidence of a role for the carbonate radical anion. *J. Am. Chem. Soc.* **132**, 17174–17185
20. Moreno, D. M., Martí, M. A., De Biase, P. M., Estrin, D. A., Demicheli, V., Radi, R., and Boechi, L. (2011) Exploring the molecular basis of human manganese superoxide dismutase inactivation mediated by tyrosine 34 nitration. *Arch. Biochem. Biophys.* **507**, 304–309
21. Radi, R. (2013) Protein tyrosine nitration: biochemical mechanisms and structural basis of functional effects. *Acc. Chem. Res.* **46**, 550–559
22. Radi, R., Beckman, J. S., Bush, K. M., and Freeman, B. A. (1991) Peroxynitrite-induced membrane lipid peroxidation: the cytotoxic potential of superoxide and nitric oxide. *Arch. Biochem. Biophys.* **288**, 481–487
23. Hughes, M. N., and Nicklin, H. G. (1970) A possible role for the species peroxynitrite in nitrification. *Biochim. Biophys. Acta* **222**, 660–661
24. Bradford, M. M. (1976) A rapid and sensitive method for the quantitation of microgram quantities of protein utilizing the principle of protein-dye binding. *Anal. Biochem.* **72**, 248–254
25. Crow, J. P., Sampson, J. B., Zhuang, Y., Thompson, J. A., and Beckman, J. S. (1997) Decreased zinc affinity of amyotrophic lateral sclerosis-associated superoxide dismutase mutants leads to enhanced catalysis of tyrosine nitration by peroxynitrite. *J. Neurochem.* **69**, 1936–1944
26. McCord, J. M., and Fridovich, I. (1969) Superoxide dismutase: an enzymic function for erythrocyte hemocuprein (hemocuprein). *J. Biol. Chem.* **244**, 6049–6055
27. Peskin, A. V., and Winterbourn, C. C. (2006) Taurine chloramine is more selective than hypochlorous acid at targeting critical cysteines and inactivating creatine kinase and glyceraldehyde-3-phosphate dehydrogenase. *Free Radic. Biol. Med.* **40**, 45–53
28. Alvarez, B., Ferrer-Sueta, G., Freeman, B. A., and Radi, R. (1999) Kinetics of peroxynitrite reaction with amino acids and human serum albumin. *J. Biol. Chem.* **274**, 842–848
29. Ellman, G. L. (1959) Tissue sulfhydryl groups. *Arch. Biochem. Biophys.* **82**, 70–77
30. Trujillo, M., Budde, H., Piñeyro, M. D., Stehr, M., Robello, C., Flohé, L., and Radi, R. (2004) *Trypanosoma brucei* and *Trypanosoma cruzi* trypanoxidoxin peroxidases catalytically detoxify peroxynitrite via oxidation of fast reacting thiols. *J. Biol. Chem.* **279**, 34175–34182
31. Brito, C., Naviliat, M., Tiscornia, A. C., Vuillier, F., Gualco, G., Dighiero, G., Radi, R., and Cayota, A. M. (1999) Peroxynitrite inhibits T lymphocyte activation and proliferation by promoting impairment of tyrosine phosphorylation and peroxynitrite-driven apoptotic death. *J. Immunol.* **162**, 3356–3366
32. Peloso, E. F., Gonçalves, C. C., Silva, T. M., Ribeiro, L. H., Piñeyro, M. D., Robello, C., and Gadelha, F. R. (2012) Trypanoxidoxin peroxidases and superoxide dismutases expression as well as ROS release are related to *Trypanosoma cruzi* epimastigotes growth phases. *Arch. Biochem. Biophys.* **520**, 117–122
33. Romero, N., Radi, R., Linares, E., Augusto, O., Detweiler, C. D., Mason, R. P., and Denicola, A. (2003) Reaction of human hemoglobin with peroxynitrite: isomerization to nitrate and secondary formation of protein radicals. *J. Biol. Chem.* **278**, 44049–44057
34. Hellman, U. (2000) Sample preparation by SDS/PAGE and in-gel digestion. *EXS* **88**, 43–54
35. Nicholls, S. J., Shen, Z., Fu, X., Levison, B. S., and Hazen, S. L. (2005) Quantification of 3-nitrotyrosine levels using a benchtop ion trap mass spectrometry method. *Methods Enzymol.* **396**, 245–266
36. Turko, I. V., and Murad, F. (2005) Mapping sites of tyrosine nitration by matrix-assisted laser desorption/ionization mass spectrometry. *Methods Enzymol.* **396**, 266–275
37. Leslie, A. G. W. (2007) Processing diffraction data with mosflm. In *Evolving Methods for Macromolecular Crystallography* (Read, R. J., and Sussman, J. L., eds) pp. 41–51, Springer, New York
38. Evans, P. (2006) Scaling and assessment of data quality. *Acta Crystallogr. D Biol. Crystallogr.* **62**, 72–82
39. Trapani, S., and Navaza, J. (2008) AMoRe: classical and modern. *Acta*

- Crystallogr. D Biol. Crystallogr.* **64**, 11–16
40. Vonrhein, C., Flensburg, C., Keller, P., Sharff, A., Smart, O., Paciorek, W., Womack, T., and Bricogne, G. (2011) Data processing and analysis with the autoPROC toolbox. *Acta Crystallogr. D Biol. Crystallogr.* **67**, 293–302
 41. Emsley, P., Lohkamp, B., Scott, W. G., and Cowtan, K. (2010) Features and development of Coot. *Acta Crystallogr. D Biol. Crystallogr.* **66**, 486–501
 42. Chen, V. B., Arendall, W. B., 3rd, Headd, J. J., Keedy, D. A., Immormino, R. M., Kapral, G. J., Murray, L. W., Richardson, J. S., and Richardson, D. C. (2010) MolProbity: all-atom structure validation for macromolecular crystallography. *Acta Crystallogr. D Biol. Crystallogr.* **66**, 12–21
 43. Cheatham, T. E., 3rd, Cieplak, P., and Kollman, P. A. (1999) A modified version of the Cornell *et al.* force field with improved sugar pucker phases and helical repeat. *J. Biomol. Struct. Dyn.* **16**, 845–862
 44. Petruk, A. A., Bartesaghi, S., Trujillo, M., Estrin, D. A., Murgida, D., Kalyanaraman, B., Marti, M. A., and Radi, R. (2012) Molecular basis of intramolecular electron transfer in proteins during radical-mediated oxidations: computer simulation studies in model tyrosine-cysteine peptides in solution. *Arch. Biochem. Biophys.* **525**, 82–91
 45. Leach, A. (2001) *Molecular Modelling: Principles and Applications*, Prentice Hall, New York
 46. Case, D., Darden, T., Cheatham, T., Simmerling, C., Wang, J., Duke, R., Luo, R., Merz, K., Pearlman, D., Crowley, M., Walker, R., Zhang, W., Wang, W., Hayik, S., Roitberg, A., Seabra, G., Wong, K., Paesani, F., Wu, X., Brozell, S., Tsui, V., Gohlke, H., Yang, L., Tan, C., Mongan, J., Hornak, V., Cui, G., Beroza, P., Mathews, D., Schafmeister, C., Ross, W., and Kollman, P. A. (2006) *AMBER 9*, University of California, San Francisco, California
 47. Beratan, D. N., Betts, J. N., and Onuchic, J. N. (1991) Protein electron transfer rates set by the bridging secondary and tertiary structure. *Science* **252**, 1285–1288
 48. Beratan, D. N., Onuchic, J. N., Winkler, J. R., and Gray, H. B. (1992) Electron-tunneling pathways in proteins. *Science* **258**, 1740–1741
 49. Shih, C., Museth, A. K., Abrahamsson, M., Blanco-Rodriguez, A. M., Di Bilio, A. J., Sudhamsu, J., Crane, B. R., Ronayne, K. L., Towrie, M., Vlcek, A., Jr., Richards, J. H., Winkler, J. R., and Gray, H. B. (2008) Tryptophan-accelerated electron flow through proteins. *Science* **320**, 1760–1762
 50. Stubbe, J., Nocera, D. G., Yee, C. S., and Chang, M. C. (2003) Radical initiation in the class I ribonucleotide reductase: long-range proton-coupled electron transfer? *Chem. Rev.* **103**, 2167–2201
 51. Alvarez-Paggi, D., Martín, D. F., DeBiase, P. M., Hildebrandt, P., Marti, M. A., and Murgida, D. H. (2010) Molecular basis of coupled protein and electron transfer dynamics of cytochrome *c* in biomimetic complexes. *J. Am. Chem. Soc.* **132**, 5769–5778
 52. Aubert, C., Mathis, P., Eker, A. P., and Brettel, K. (1999) Intraprotein electron transfer between tyrosine and tryptophan in DNA photolyase from *Anacystis nidulans*. *Proc. Natl. Acad. Sci. U.S.A.* **96**, 5423–5427
 53. Ly, H. K., Marti, M. A., Martín, D. F., Alvarez-Paggi, D., Meister, W., Kranich, A., Weidinger, I. M., Hildebrandt, P., and Murgida, D. H. (2010) Thermal fluctuations determine the electron-transfer rates of cytochrome *c* in electrostatic and covalent complexes. *Chemphyschem* **11**, 1225–1235
 54. Li, H., Robertson, A. D., and Jensen, J. H. (2005) Very fast empirical prediction and rationalization of protein pK_a values. *Proteins* **61**, 704–721
 55. Bas, D. C., Rogers, D. M., and Jensen, J. H. (2008) Very fast prediction and rationalization of pK_a values for protein-ligand complexes. *Proteins* **73**, 765–783
 56. Olsson, M. H. M., Søndergaard, C. R., Rostkowski, M., and Jensen, J. H. (2011) PROPKA3: consistent treatment of internal and surface residues in empirical pK_a predictions. *J. Chem. Theory Comput.* **7**, 525–537
 57. Søndergaard, C. R., Olsson, M. H. M., Rostkowski, M., and Jensen, J. H. (2011) Improved treatment of ligands and coupling effects in empirical calculation and rationalization of pK_a values. *J. Chem. Theory Comput.* **7**, 2284–2295
 58. Taylor, M. C., and Kelly, J. M. (2006) pTcINDEX: a stable tetracycline-regulated expression vector for *Trypanosoma cruzi*. *BMC Biotechnol.* **6**, 32
 59. Piacenza, L., Peluffo, G., Alvarez, M. N., Kelly, J. M., Wilkinson, S. R., and Radi, R. (2008) Peroxiredoxins play a major role in protecting *Trypanosoma cruzi* against macrophage- and endogenously-derived peroxynitrite. *Biochem. J.* **410**, 359–368
 60. Wilkinson, S. R., Prathalingam, S. R., Taylor, M. C., Ahmed, A., Horn, D., and Kelly, J. M. (2006) Functional characterisation of the iron superoxide dismutase gene repertoire in *Trypanosoma brucei*. *Free Radic. Biol. Med.* **40**, 198–209
 61. Forman, H. J., and Fridovich, I. (1973) Superoxide dismutase: a comparison of rate constants. *Arch. Biochem. Biophys.* **158**, 396–400
 62. Crow, J. P., Beckman, J. S., and McCord, J. M. (1995) Sensitivity of the essential zinc-thiolate moiety of yeast alcohol dehydrogenase to hypochlorite and peroxynitrite. *Biochemistry* **34**, 3544–3552
 63. Zou, M. H., Daiber, A., Peterson, J. A., Shoun, H., and Ullrich, V. (2000) Rapid reactions of peroxynitrite with heme-thiolate proteins as the basis for protection of prostacyclin synthase from inactivation by nitration. *Arch. Biochem. Biophys.* **376**, 149–155
 64. Ferrer-Sueta, G., and Radi, R. (2009) Chemical biology of peroxynitrite: kinetics, diffusion, and radicals. *ACS Chem. Biol.* **4**, 161–177
 65. Radi, R. (2004) Nitric oxide, oxidants, and protein tyrosine nitration. *Proc. Natl. Acad. Sci. U.S.A.* **101**, 4003–4008
 66. Tien, M., Berlett, B. S., Levine, R. L., Chock, P. B., and Stadtman, E. R. (1999) Peroxynitrite-mediated modification of proteins at physiological carbon dioxide concentration: pH dependence of carbonyl formation, tyrosine nitration, and methionine oxidation. *Proc. Natl. Acad. Sci. U.S.A.* **96**, 7809–7814
 67. Denicola, A., Freeman, B. A., Trujillo, M., and Radi, R. (1996) Peroxynitrite reaction with carbon dioxide/bicarbonate: kinetics and influence on peroxynitrite-mediated oxidations. *Arch. Biochem. Biophys.* **333**, 49–58
 68. Lymar, S. V., and Hurst, J. K. (1996) Carbon dioxide: physiological catalyst for peroxynitrite-mediated cellular damage or cellular protectant? *Chem. Res. Toxicol.* **9**, 845–850
 69. Pryor, W. A., Lemercier, J. N., Zhang, H., Uppu, R. M., and Squadrito, G. L. (1997) The catalytic role of carbon dioxide in the decomposition of peroxynitrite. *Free Radic. Biol. Med.* **23**, 331–338
 70. Koppenol, W. H., and Kissner, R. (1998) Can O=NOOH undergo homolysis? *Chem. Res. Toxicol.* **11**, 87–90
 71. Koppenol, W. H., Moreno, J. J., Pryor, W. A., Ischiropoulos, H., and Beckman, J. S. (1992) Peroxynitrite, a cloaked oxidant formed by nitric oxide and superoxide. *Chem. Res. Toxicol.* **5**, 834–842
 72. Ford, E., Hughes, M. N., and Wardman, P. (2002) Kinetics of the reactions of nitrogen dioxide with glutathione, cysteine, and uric acid at physiological pH. *Free Radic. Biol. Med.* **32**, 1314–1323
 73. Reiter, C. D., Teng, R. J., and Beckman, J. S. (2000) Superoxide reacts with nitric oxide to nitrate tyrosine at physiological pH via peroxynitrite. *J. Biol. Chem.* **275**, 32460–32466
 74. Sawa, T., Akaike, T., and Maeda, H. (2000) Tyrosine nitration by peroxynitrite formed from nitric oxide and superoxide generated by xanthine oxidase. *J. Biol. Chem.* **275**, 32467–32474
 75. Abriata, L. A., Cassina, A., Tórtora, V., Marín, M., Souza, J. M., Castro, L., Vila, A. J., and Radi, R. (2009) Nitration of solvent-exposed tyrosine 74 on cytochrome *c* triggers heme iron-methionine 80 bond disruption: nuclear magnetic resonance and optical spectroscopy studies. *J. Biol. Chem.* **284**, 17–26
 76. Bacheга, J. F., Navarro, M. V., Bleicher, L., Bortoleto-Bugs, R. K., Dive, D., Hoffmann, P., Viscogliosi, E., and Garratt, R. C. (2009) Systematic structural studies of iron superoxide dismutases from human parasites and a statistical coupling analysis of metal binding specificity. *Proteins* **77**, 26–37
 77. Boucher, I. W., Brzozowski, A. M., Brannigan, J. A., Schnick, C., Smith, D. J., Kyes, S. A., and Wilkinson, A. J. (2006) The crystal structure of superoxide dismutase from *Plasmodium falciparum*. *BMC Struct. Biol.* **6**, 20
 78. Guan, Y., Hickey, M. J., Borgstahl, G. E., Hallewell, R. A., Lepock, J. R., O'Connor, D., Hsieh, Y., Nick, H. S., Silverman, D. N., and Tainer, J. A. (1998) Crystal structure of Y34F mutant human mitochondrial manganese superoxide dismutase and the functional role of tyrosine 34. *Biochemistry* **37**, 4722–4730
 79. Reece, S. Y., Hodgkiss, J. M., Stubbe, J., and Nocera, D. G. (2006) Proton-coupled electron transfer: the mechanistic underpinning for radical transport and catalysis in biology. *Philos. Trans. R. Soc. Lond B Biol. Sci.* **361**, 1351–1364

Peroxynitrite-mediated Inactivation of *T. cruzi* Fe-SODs

80. Bhattacharjee, S., Deterding, L. J., Jiang, J., Bonini, M. G., Tomer, K. B., Ramirez, D. C., and Mason, R. P. (2007) Electron transfer between a tyrosyl radical and a cysteine residue in hemoproteins: spin trapping analysis. *J. Am. Chem. Soc.* **129**, 13493–13501
81. Witting, P. K., and Mauk, A. G. (2001) Reaction of human myoglobin and H₂O₂. Electron transfer between tyrosine 103 phenoxyl radical and cysteine 110 yields a protein-thiyl radical. *J. Biol. Chem.* **276**, 16540–16547
82. Giese, B., Graber, M., and Cordes, M. (2008) Electron transfer in peptides and proteins. *Curr. Opin. Chem. Biol.* **12**, 755–759
83. Cordes, M., Köttgen, A., Jasper, C., Jacques, O., Boudebous, H., and Giese, B. (2008) Influence of amino acid side chains on long-distance electron transfer in peptides: electron hopping via “stepping stones”. *Angew Chem. Int. Ed. Engl.* **47**, 3461–3463
84. Graceffa, P. (1983) Spin labeling of protein sulfhydryl groups by spin trapping a sulfur radical: application to bovine serum albumin and myosin. *Arch. Biochem. Biophys.* **225**, 802–808
85. Maples, K. R., Jordan, S. J., and Mason, R. P. (1988) *In vivo* rat hemoglobin thiyl free radical formation following administration of phenylhydrazine and hydrazine-based drugs. *Drug Metab. Dispos.* **16**, 799–803
86. Gatti, R. M., Radi, R., and Augusto, O. (1994) Peroxynitrite-mediated oxidation of albumin to the protein-thiyl free radical. *FEBS Lett.* **348**, 287–290
87. Carballal, S., Bartsaghi, S., and Radi, R. (2014) Kinetic and mechanistic considerations to assess the biological fate of peroxynitrite. *Biochim. Biophys. Acta* **1840**, 768–780
88. Fasman, G. D. (1976). in *Handbook of Biochemistry and Molecular Biology: Physical Data and Chemical Data*, pp. 305–351, CRC Press, Inc., Cleveland, OH
89. Radi, R. (2013) Peroxynitrite, a stealthy biological oxidant. *J. Biol. Chem.* **288**, 26464–26472
90. Quint, P., Reutzel, R., Mikulski, R., McKenna, R., and Silverman, D. N. (2006) Crystal structure of nitrated human manganese superoxide dismutase: mechanism of inactivation. *Free Radic. Biol. Med.* **40**, 453–458
91. Ischiropoulos, H., Zhu, L., Chen, J., Tsai, M., Martin, J. C., Smith, C. D., and Beckman, J. S. (1992) Peroxynitrite-mediated tyrosine nitration catalyzed by superoxide dismutase. *Arch. Biochem. Biophys.* **298**, 431–437
92. Adams, P. D., Afonine, P. V., Bunkóczi, G., Chen, V. B., Davis, I. W., Echols, N., Headd, J. J., Hung, L. W., Kapral, G. J., Grosse-Kunstleve, R. W., McCoy, A. J., Moriarty, N. W., Oeffner, R., Read, R. J., Richardson, D. C., Richardson, J. S., Terwilliger, T. C., and Zwart, P. H. (2010) PHENIX: a comprehensive Python-based system for macromolecular structure solution. *Acta Crystallogr. D Biol. Crystallogr.* **66**, 213–221